Computer Experiments on Rapidly Rotating Plane Couette Flow

Mustafa Barri* and Helge I. Andersson

Fluids Engineering Division, Department of Energy and Process Engineering, Norwegian University of Science and Technology, 7491 Trondheim, Norway.

Abstract. The turbulence in plane Couette flow subjected to system rotation is investigated. The anti-cyclonic rotation rate is well above the range in which roll-cells occur and close to the upper bound, beyond which no stationary turbulent states of motion exist. The mean velocity profile exhibits a linear region over 80% of the cross-section, in which the mean absolute vorticity is driven to zero. Viscous effects still prevail in narrow regions next to the walls, whereas the quasi-homogeneous central core exhibits abnormal anisotropies of the Reynolds stress tensor, the vorticity tensor and the energy dissipation rate tensor. In spite of the distinctly higher turbulence level observed, a 13% drag reduction is found. This paradoxical finding is ascribed to configurational changes in the turbulence field brought about by the system rotation.

AMS subject classifications: 76M12, 76F10, 76F65, 76U05

Key words: Turbulence, plane Couette flow, system rotation, anti-cyclonic rotation, anisotropy tensor, zero absolute mean vorticity.

1 Introduction

Rotation might give rise to remarkable and profound alterations of shear flow turbulence. Ever since the illuminating experimental investigation of a rotating plane channel flow by Johnston *et al.* [20], it has been known that the action of the Coriolis force due to system rotation changes not only the mean velocity distribution but also the turbulent velocity fluctuations. The location of maximum mean velocity is shifted from the channel center towards the so-called '*suction*' side, and the mean velocity profile exhibits a linear region with slope close to twice the imposed rotation rate. The turbulence intensity is reduced

---

*Corresponding author. *Email addresses:* `mustafa.barri@ntnu.no` (M. Barri), `helge.i.andersson@ntnu.no` (H. I. Andersson)

or sometimes even suppressed near this '*suction*' side, whereas the turbulent agitation is enhanced at the opposite side of the channel, i.e., along '*pressure*' side. These essential observations have later been confirmed and supplemented by more recent experimental studies by Nakabayashi and Kitoh [30, 31] and direct numerical simulations by Kristof-fersen and Andersson [22], Lamballais *et al.* [23, 24], Liu and Lu [26] and Grundestam *et al.* [13].

The influence of the Coriolis force due to imposed system rotation depends both on the orientation and the magnitude of the background vorticity $2\Omega^F$ relative to the mean flow vorticity $\mathbf{\Omega} \equiv \nabla \times \mathbf{u}$ in a rotating frame-of-reference. In simple shear flows, like the two-dimensional channel flow, the mean vorticity vector $\mathbf{\Omega}$ is perpendicular to both the mean flow direction, say x, and to the wall-normal direction, say y. If the angular velocity vector $\mathbf{\Omega}^F$ of the rotating frame-of-reference is aligned with $\mathbf{\Omega}$, the local vorticity ratio $S \equiv 2\Omega^F/\Omega$ effectively distinguishes between different flow regimes. In the plane channel flow, for instance, S changes sign where the mean velocity peaks and the rotating channel flow is therefore simultaneously affected by cyclonic ($S > 0$) and anti-cyclonic ($S < 0$) rotation.

In contrast with the pressure-driven plane channel flow, the shear-driven plane Couette flow exhibits a monotonically increasing mean velocity from one wall to the other with the obvious implication that the entire flow field is either exposed to cyclonic or anti-cyclonic rotation. This fact alone makes the rotating plane Couette flow an attractive prototype for explorations of rotational effects on rotating shear flows. In this context, the notion of '*pressure*' and '*suction*' sides should be discarded. Hart [15] found that the *laminar* plane Couette flow is unstable with respect to inception of counter-rotating roll cells in the parameter range $-1 < S < 0$ and otherwise stable. In the *turbulent* flow regime, the mean flow vorticity Ω is no longer constant across the flow and S varies with the distance from the wall. Bech and Andersson [6] therefore introduced a rotation number defined in terms of the average mean flow vorticity Ω_{av}, i.e., $Ro \equiv -2\Omega^F/\Omega_{av}$. Here, Ω_{av} also equals the constant vorticity of the corresponding laminar Couette flow. Care should be taken not to mix up the rotation number defined above with the Rossby number routinely used in geophysical fluid dynamics.

In a computational study of turbulent plane Couette flow, Bech and Andersson [6] observed that the roll cell instability was present also in the turbulent case provided that the rotation is anti-cyclonic ($Ro = +0.01$). If the Couette flow, on the other hand, was sub-jected to weak cyclonic rotation with $Ro = -0.01$, no roll cells appeared and the turbulence was damped as compared with the turbulence level in non-rotating Couette flow. At the same time laboratory investigations by Tillmark and Alfredsson [37] and computer simulations by Komminaho *et al.* [21] showed that cyclonic rotation may completely suppress the turbulence.

While Bech and Andersson [6] were concerned about weak rotation with a rotation number $Ro = \pm 0.01$, the intermediate rotation numbers $Ro = 0.10, 0.20$ and 0.50 were considered in a subsequent study by Bech and Andersson [7]. The weak but yet distinct roll cells observed already at $Ro = +0.01$ became more regular and energetic at $Ro = +0.10$ and

$+0.20$. At the highest rotation rate $Ro=+0.50$, however, a disordering of the counter-rotating vortices appeared. The overall turbulence level was substantially higher than in the non-rotating flow and the resulting skin-friction was roughly 20% above that for $Ro=0$.

Bech and Andersson [7] also attempted to simulate the anti-cyclonically rotating Couette flow with $Ro=+1.0$ and reported that the turbulent fluctuations were completely suppressed and the flow laminarized. This finding is consistent with the more recent observations by Alfredsson and Tillmark [1]. Their flow visualization studies revealed that the distinct roll cells observed at $Ro=+0.50$ were also distinguishable at $Ro=+0.75$. For rotation numbers above $+0.75$, however, they claim that the predominant cell structures have vanished and the elongation of the turbulent structures was significant. For $Ro>+1.0$ the turbulence was quenched, no roll cells were seen, and the flow was fully laminarized.

The central core region of a rotating Couette flow bears some resemblances with homogeneous shear flow subjected to system rotation. Rotating homogeneous shear flows have been considered both theoretically and numerically, including the computer simulations by Bartello *et al.* [5], Salhi and Cambon [35], Yanase *et al.* [40], Brethouwer [9] and Iida *et al.* [16]. Rotating homogeneous shear flows are known to be neutrally stable if the vorticity ratio $S=-1.0$ [11,35]. This special case of anti-cyclonic rotation with $S=-1.0$, i.e., *zero absolute mean vorticity*, is particularly interesting. According to the Bradshaw-Richardson number $B=S(S+1)$, the case $S=-1$ should be neutrally stable (i.e., $B=0$) just as the non-rotating case $S=0$. Cambon *et al.* [11] convincingly demonstrated that although the zero absolute mean vorticity case should be equivalent to the $S=0$ case according to the Bradshaw-Richardson stability criterion, the flow dynamics are indeed strikingly different. Comprehensive support of this view has subsequently been provided by Salhi and Cambon [35] and Brethouwer [9]. Yanase *et al.* [40] and Brethouwer [9] found that the flow field was dominated by very elongated and intense streamwise vortex tubes. Iida *et al.* [16] focused on $S=\pm0.5$ with the view to investigate the tilting mechanism of the longitudinal vortex structures. Here, anti-cyclonic rotation $S=-1/2$ corresponds to *zero-tilting vorticity* and maximum destabilization ($B=-1/4$) according to Cambon *et al.* [11]. Iida *et al.* [16] examined the influence of spanwise system rotation on the vertical flow structures and observed that the spanwise tilting of the structures was reduced whereas their inclination with respect to the mean flow direction was increased.

It is well known that the rotating plane Couette flow can be considered as the narrow-gap limit of the Taylor-Couette (TC) flow, i.e., the fluid motion in the annular gap between two independently rotating circular cylinders; see, e.g., Dubrulle *et al.* [12]. A wealth of stable flow regimes was observed in the TC apparatus of Andereck *et al.* [2], several of which exhibited toroidal Taylor vortices analogous to the roll cells observed by Bech and Andersson [7] and Alfredsson and Tillmark [1] in the rotating plane Couette flow. Townsend [38] assumed two different kinds of TC turbulence, one generated by the mean shear and the other due to the Taylor-vortices. In *featureless turbulence*, i.e., turbulence

devoid of any sustained large-scale features, only the shear mechanism is retained. Such featureless turbulence was also observed in the Taylor-Couette flow by Andereck *et al.* [2] in a certain parameter range.

The purpose of the present study is to identify, if possible, a plane Couette flow subjected to sufficiently strong anti-cyclonic rotation such that the roll-cell instability is completely suppressed but the turbulence still persists. If so, this particular flow configuration offers a unique environment in which the influence of the Coriolis force due to system rotation on shear flow turbulence can be studied in isolation, i.e., without being hampered by the simultaneous occurrence of roll cells. Unlike the featureless turbulence occurring in the Taylor-Couette flow, the plane Couette flow turbulence is unaffected by streamline curvature which inevitably affects the TC-flow, see, e.g., Patel and Sotiropoulos [33].

First, the fully developed turbulent plane Couette flow in orthogonal-mode rotation is defined in Section 2 and some fundamental conservation laws in rotating frames-of-reference are provided. The basics of the direct numerical simulations performed are provided in Section 3. The primary flow statistics and Reynolds stress budgets are presented in Sections 4 and 5, respectively, while vortex dynamics and flow anisotropies are considered in Sections 6-7.

2   Orthogonally rotating plane Couette flow

2.1   Flow configuration and governing equations

Let us consider the turbulent Couette flow driven in the x-direction by the relative motion of two infinite parallel planes separated a distance $2h$ in the y-direction. The fluid motion is induced solely by the prescribed velocity difference $2U_w$ between the two planes (see Fig. 1). The flow is characterized by the Reynolds number $Re \equiv \rho U_w h / \mu$, where ρ and μ are the density and the dynamic viscosity of the incompressible fluid, respectively. The shear-driven Couette flow is rotated about the spanwise z-axis with constant angular velocity $\mathbf{\Omega}^F = (0,0,\Omega^F)$. Since the average mean vorticity Ω_{av} is $-U_w/h$, the rotation number becomes:

$$Ro \equiv -2\Omega^F/\Omega_{av} = 2\Omega^F h/U_w. \tag{2.1}$$

The incompressible flow of a Newtonian fluid in a constantly rotating frame-of-reference is governed by the conservation equations for mass and momentum:

$$\nabla \cdot \boldsymbol{u} = 0, \tag{2.2a}$$

$$\frac{\partial \boldsymbol{u}}{\partial t} + \boldsymbol{u} \cdot \nabla \boldsymbol{u} = -\frac{1}{\rho} \nabla p + \nu \nabla^2 \boldsymbol{u} - 2\boldsymbol{\Omega}^F \times \boldsymbol{u}, \tag{2.2b}$$

where ν is the kinematic viscosity μ/ρ. The last term on the right-hand side of Eq. (2.2b) is the Coriolis force due to system rotation, whereas centrifugal effects are absorbed in the effective pressure p. Since both U_w and Ω^F are prescribed constants, the time-dependent
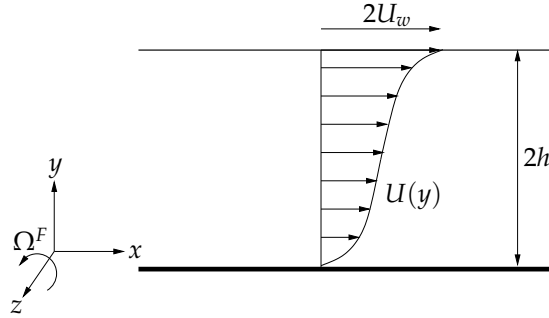
Figure 1: Schematic of spanwise rotating plane Couette flow. The system is rotating with constant angular velocity Ω^F about the spanwise z-axis.

flow field will eventually evolve into a statistically steady state which is the subject of the present investigation.

2.2 Reynolds' decomposition

The instantaneous velocity components u_i and pressure p can be decomposed into mean (U_i, P) and fluctuating (u_i, p) parts to facilitate both the presentation and interpretation of the outcome of the simulation. In the absence of rotational-induced roll cells, the mean flow becomes unidirectional $(U, 0, 0)$ and the mean pressure P serves primarily to balance the wall-normal component of the Coriolis force:

$$\frac{1}{\rho}\frac{dP}{dy} = -2\Omega^F U - \frac{d}{dy}\overline{v^2}. \tag{2.3}$$

This balance results from the Reynolds-average of Eq. (2.2b) in the y-direction, provided that the flow is statistically homogenous in (x, z)-planes. If the corresponding mean momentum equation in the x-direction is integrated once in y, the constancy of the total mean shear stress:

$$\mu\frac{dU}{dy} - \rho\overline{uv} = \tau_w \equiv \rho u_\tau^2 \tag{2.4}$$

is obtained. Here, u_τ denotes the wall-friction velocity. It is noteworthy that the sum of the viscous and turbulent shear stresses remains constant throughout the flow field, irrespective of whether the flow is rotating or not. This is so because the mean flow U is only affected indirectly by the Coriolis force through the turbulent or Reynolds shear stress $-\rho\overline{uv}$. The latter is governed by the transport equation for the individual second-moments:

$$\frac{D\overline{u_i u_j}}{Dt} = P_{ij} + G_{ij} + D_{ij} + \Pi_{ij} - \varepsilon_{ij}. \tag{2.5}$$

The right-hand-side terms, which are responsible for production due to mean shear (P_{ij}), production due to rotation (G_{ij}), viscous and turbulent diffusion (D_{ij}), pressure-strain redistribution (Π_{ij}), and viscous energy dissipation (ε_{ij}), are defined in the Appendix.

The mean turbulent kinetic energy $k \equiv \frac{1}{2}\overline{u_i u_i}$ is a convenient scalar measure of the turbulent activity. The one-to-one relationship (2.4) between the viscous and turbulent shear stress components makes it possible to express the production of mean turbulent kinetic energy P_K in terms of only the mean shear rate:

$$P_K \equiv \frac{1}{2}P_{ii} = \frac{1}{2}P_{xx} = -\overline{uv}\frac{dU}{dy} = \frac{u_\tau^4}{\nu}\left(1 - \frac{dU^+}{dy^+}\right)\frac{dU^+}{dy^+}. \tag{2.6}$$

Here, U^+ and y^+ are the inner or wall variables U/u_τ and yu_τ/ν, respectively. Maximum production is obtained where $dU^+/dy^+ = 1/2$, which according to Eq. (2.4) is the location at which the viscous and turbulent shear stress components are equal. Eq. (2.6) for the production P_K of mean turbulent kinetic energy also shows that the production $P_K = 0$ as long as $dU^+/dy^+ = 1$, i.e., in the innermost viscous sublayer where the mean velocity varies linearly with the distance from the wall. This turns out to be an exact result for the plane Couette flow, whereas the same is only approximately correct in channel flows.

2.3 Mean vorticity and second-moments of vorticity fluctuations

The components of the instantaneous vorticity vector are decomposed in mean Ω_i and fluctuating ω_i parts in accordance with the Reynolds decomposition. In the present case where the steady mean flow is unidirectional and the turbulence statistics are homogeneous in (x,z)-planes and in time, the equation for the only non-vanishing mean vorticity component $\Omega_z = -dU/dy$ reduces to the ordinary differential equation:

$$0 = \frac{d}{dy}\left(\overline{w\omega_y} - \overline{v\omega_z}\right) + \nu\frac{d^2\Omega_z}{dy^2}, \tag{2.7}$$

which can be integrated once to give:

$$0 = \overline{w\omega_y} - \overline{v\omega_z} + \nu\frac{d\Omega_z}{dy}. \tag{2.8}$$

Here, the constant of integration is zero since all the terms vanish identically at both walls. It is noteworthy that the vorticity $2\Omega^F$ due to the imposed system rotation does not appear explicitly in Eq. (2.7). This is so because we are concerned only with orthogonal mode rotation, i.e., the axis of rotation is aligned with the mean strain rate vector. This particular orientation of the imposed rotation does not contribute to stretching and/or tilting of the mean vorticity by mean strain.

Transport for the individual second-moments of the vorticity fluctuations can written symbolically as:

$$\frac{D\overline{\omega_i\omega_j}}{Dt} = T1_{ij} + T2_{ij} + S3_{ij} + S4_{ij} + S5_{ij} + V6_{ij} + V7_{ij}, \tag{2.9}$$

where the terms on the right-hand side are given in the Appendix. The terms are numbered according to their order of appearance in Tennekes and Lumley [36] and Antonia and Kim [3]. Their enstrophy budgets are readily recovered as half the trace of Eq. (2.9). The capital letters are used to distinguish between transport (T), stretching (S) and viscous (V) terms. In the equation above, the system rotation appears explicitly only in the third stretching term $S5_{ij}$.

A striking difference between the second-moment equation for the velocity fluctuations (2.5) and that for the vorticity fluctuations (2.9) should be pointed out. While Eq. (2.5) simplifies considerably upon contraction of the indices since both $\Pi_{ii} = 0$ and $G_{ii} = 0$, none of the terms vanish when Eq. (2.9) is contracted to the enstrophy budget. In the present context, it is particularly noteworthy that the effect of system rotation remains in the stretching terms $S5_{ii}$ also after contraction. The enstrophy is therefore explicitly influenced by rotation, in contrast with the turbulent kinetic energy.

3 Computer simulations

A direct numerical simulation of a fully developed Couette flow at $Re = 1300$ and $Ro = 0.7$ has been performed. This Reynolds number is the same as that considered by Bech *et al.* [8] and Bech and Andersson [6,7], which is well above 500 as required for fully developed turbulence to persist [1]. The second-order accurate finite-volume code MGLET [28], was used for the numerical integration of the incompressible Navier-Stokes equations (2.2). The pressure is defined at the center of each grid cell and the velocity components at the interfaces. The velocity components and their derivatives are obtained by linear interpolation and central differences, respectively. An explicit second-order Adams-Bashforth scheme was employed for the time integration. Periodic boundary conditions were used in the two homogeneous directions and no-slip and impermeability conditions were imposed at both walls. The simulations were run on a parallel MPI computer.

The length and width of the computational domain were $L_x = 28\pi h$ and $L_z = 4\pi h$, and the number of grid points was $896 \times 240 \times 240$ in the x-, y- and z-directions, respectively. This domain is nearly three times longer than that used by Bech *et al.* [8] and Bech and Andersson [6, 7]. The resolution in wall-units achieved by this grid for $Ro = 0.7$ corresponded to $\Delta x^+ = 7.5$ and $\Delta z^+ = 4.0$ in the two homogeneous directions whereas Δy^+ varied from 0.15 to 1.14 in the wall-normal direction. Statistical averaging was made in the two homogeneous directions and over a time interval $30h/u_\tau$. Preliminary results obtained with a smaller domain and coarser mesh were presented by Barri and Andersson [4].

For comparative purposes, a new simulation of the non-rotating Couette flow at $Re = 1300$ was performed using exactly the same computational domain and the same grid as for the $Ro = 0.7$ case. In order to eliminate the potential role of domain size and grid resolution on the results, data from the new $Ro = 0$ simulation will be used as the reference case throughout this paper to demonstrate the effects of system rotation. Comparisons
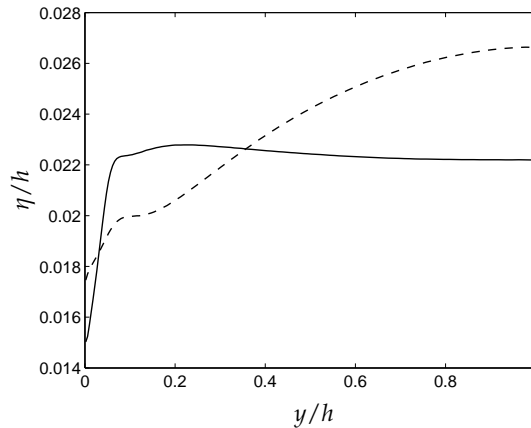
Figure 2: Kolmogorov length scale η/h for the rotating case $Ro=0.7$ (solid line) compared with the corresponding non-rotating Couette flow (broken line).

with the DNS data of Bech *et al.* [8] will be provided only for the mean velocity and the Reynolds stress profiles in Section 4.

The Kolmogorov length scale $\eta = (\nu^3/\epsilon)^{1/4}$ is a measure of the order of magnitude of the size of the smallest turbulent eddies. In anticipation of small-scale isotropy, η is a scalar quantity. Fig. 2 shows the Kolmogorov scale evaluated on the basis of the scalar dissipation rate ϵ of the mean turbulent kinetic energy. Since $\epsilon = \frac{1}{2}\varepsilon_{ii}$ varies across the flow, also η varies with y/h. While η increases with the wall distance from $0.018h$ to $0.026h$ in the non-rotating case, η exhibits a surprisingly constant level of about $0.022h$ except in the innermost 10% of the rotating Couette channel. It is worthwhile to point out that if the Kolmogorov length scale η is expressed in wall units, i.e., $\eta^+ = Re_\tau \eta/h$, we find that $\eta^+ \approx 2$ which suggests that the grid resolution used in the present simulations is fully adequate.

In order to see whether or not counter-rotating roll cells, as observed both by Bech and Andersson [7] and Tillmark and Alfredsson [37] at relatively high anti-cylonic rotation rates, are embedded in the three-dimensional flow field, the two-point correlations $R_{ij}(r_k)$ are shown in Fig. 3, in which also results for the non-rotating case are included. The non-oscillatory behaviour of $R_{22}(r_z)$ and $R_{33}(r_z)$ and the rapid decay to zero of $R_{22}(r_x)$ and $R_{33}(r_x)$ assure that the present flow field with $Ro=0.7$ does not possess any counter-rotating roll cells.

While Alfredsson and Tillmark [1] observed elongated turbulent structures and weaker roll-cells of varying spanwise extent when the rotation number was increased from 0.50 to 0.75, the present DNS at $Ro=0.70$ showed no roll cells at all. The fact that the quenching of the roll-cells at high anti-cyclonic rotation rates occurred at a somewhat lower rotation number than in the laboratory channel might be due to the lower Reynolds number $(Re=790)$ in their study or more likely due to their finite-length channel width and the relatively low aspect ratio (about 5) which implies that side-wall effects may play a role.
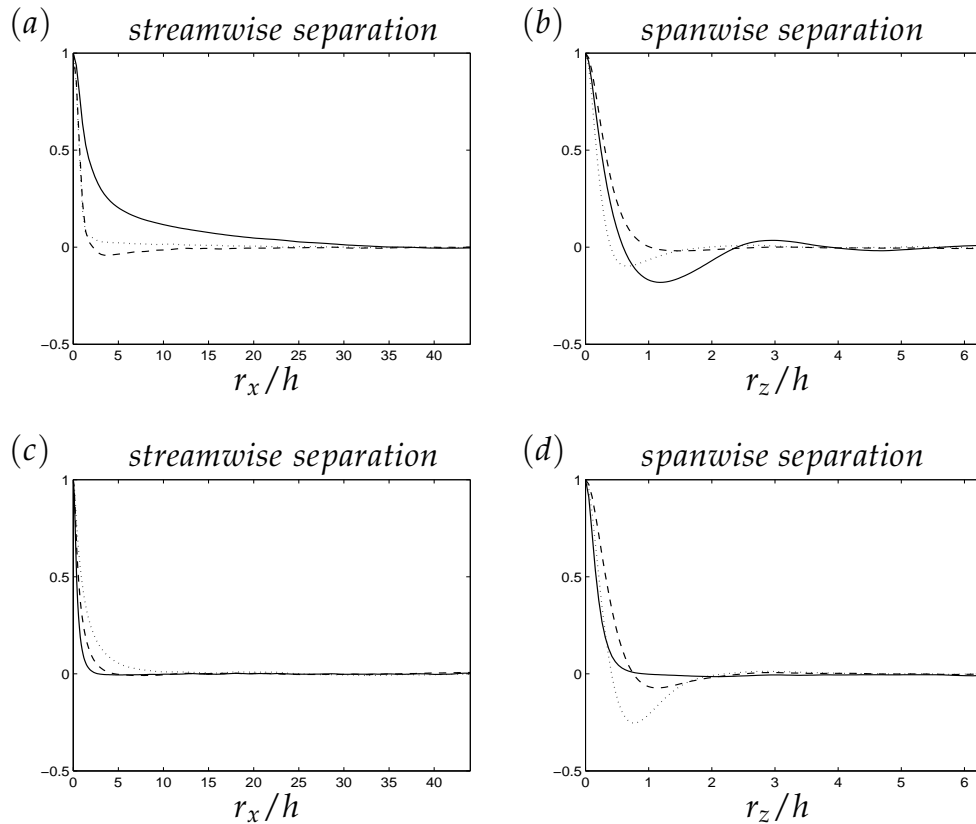
Figure 3: Two-point correlations near the center ($y/h\!=\!0.98$) with (a), (c) streamwise and (b), (d) spanwise separations. Results without rotation ($Ro\!=\!0$) are at the top and with rotation ($Ro\!=\!0.7$) are at the bottom. (——) R_{uu}; ($\cdots$) R_{vv}; (– – –) R_{ww}.

The presence of extraordinarily long flow structures in plane Couette flow [21, 39] makes the required length L_x of the computational domain substantially larger than that needed in a channel flow simulation. The two-point correlations presented in Fig. 3 show that both the length L_x and the width L_z used herein are sufficient to accommodate the largest flow structures, both in the rotating and the non-rotating Couette flow. It is also noteworthy from Fig. 3(c) that the length scale of the wall-normal fluctuations is substantially larger than the length scale of the streamwise velocity fluctuations. This is just the opposite of the situation in channel and Couette flow without rotation (see Fig. 3(a)) and is a first indication of the anomalies of rapidly rotating Couette flow.

4 Mean flow and velocity statistics

The shape of the mean velocity profile $U(y)$ in Fig. 4 is rather different from the typical S-shaped velocity distribution observed by Bech *et al.* [8] and others in non-rotating Couette
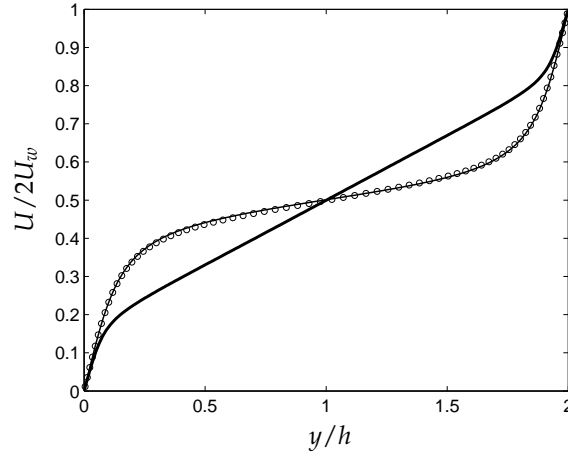
Figure 4: Mean velocity distribution $U(y)$ for $Ro = 0.7$ (bold line) compared with the corresponding profile for non-rotating Couette flow (thin line) and DNS data from [8] for $Ro = 0$ (symbols).

flow. The DNS data from Bech *et al.* [8] are included here and in the two subsequent figures simply to demonstrate the close resemblance between the present simulation for $Ro = 0$ and that of Bech *et al.* [8].

For the anti-cyclonically rotating Couette flow, the mean velocity profile exhibits a substantial linear range which extends over 80% of the cross-section. The slope dU/dy of the velocity profile in the linear region is close to $2\Omega^F$, which makes the local vorticity ratio $S \approx -1$. This shows that the mean velocity profile has adjusted itself such that the mean flow vorticity Ω just counterbalances the imposed anti-cyclonic background vorticity $2\Omega^F$, i.e., the absolute vorticity in an inertial frame-of-reference is driven to zero. This phenomenon has been observed before, both in rotating channel flows by Johnston *et al.* [20], Kristoffersen and Andersson [22], Lamballais *et al.* [23, 24] and Nakabayashi and Kitoh [30, 31] and in rotating Couette flows by Bech and Andersson [7].

The wall-friction velocity u_τ defined in Eq. (2.4) is obtained as a part of the numerical solution. Since the turbulent shear stress $-\rho\overline{uv}$ vanishes identically at the walls, u_τ is determined by the wall-slope of the mean velocity profile. The Reynolds number $Re_\tau \equiv \rho u_\tau h/\mu$ based on the wall-friction velocity u_τ is an essential dimensionless parameter, which in the present case becomes ≈ 76.5. This is significantly lower than $Re_\tau = 82.02$ found for $Ro = 0$ and $Re_\tau = 82.2$ reported by Bech *et al.* [8] for non-rotating Couette flow at the same Reynolds number. This implies that a drag reduction of about 13% has been achieved by the imposed rotation. On the contrary, at the highest rotation number $Ro = 0.5$ considered by Bech and Andersson [7] the wall-friction Reynolds number was $Re_\tau = 91.0$, i.e., a 21% increase in wall-friction.

The extent of the Coriolis-dominated region in Fig. 4 is consistent with the criterion proposed by Nakabayashi and Kitoh [30] that system rotation matters when $y > \delta_c$, where δ_c is the Coriolis length scale $\delta_c = u_\tau/\Omega^F$. In the present case, this criterion can be ex-

pressed as

$$\frac{y}{h} > \frac{2}{Ro}\frac{Re_\tau}{Re} \approx 0.2. \tag{4.1}$$

The inequality (4.1) suggests that the region in which system rotation is a leading-order effect expands with increasing rotation Ro.

Nakabayashi and Kitoh [30] argued that the Coriolis force may penetrate deep into the near-wall layer. The role played by the Reynolds number is taken over by a new dimensionless parameter, namely the ratio between the viscous length scale ν/u_τ and the Coriolis length scale u_τ/Ω^F, i.e., $\nu\Omega^F/u_\tau^2$. This new dimensionless group can readily be expressed as a combination of the rotation number and the Reynolds number as:

$$\frac{\nu\Omega^F}{u_\tau^2} = \frac{1}{2}RoReRe_\tau^{-2}. \tag{4.2}$$

In the present case of a rapidly rotating Couette flow, this group is about 0.07. In the laboratory experiments of rotating channel flow reported by Nakabayashi and Kitoh [30,31] this parameter did not exceed 0.01, whereas Kristoffersen and Andersson [22] reached about 0.02 at their highest rotation rate. The case considered herein is therefore undoubtedly one of strong rotation. The present results support the relevance of the dimensional group in Eq. (4.2) as a distinguishing parameter in rotating shear flow. While Nakabayashi and Kitoh [30] introduced this parameter as the ratio between the viscous length scale and the Coriolis length scale, the parameter can equally well be identified as the ratio between the viscous time scale ν/u_τ^2 and the Coriolis time scale $1/\Omega^F$.

It is obvious that dU/dy cannot exceed U_w/h in the Couette flow and this intuitive constraint inevitably implies that $Ro=1$ is an upper bound for which neutral stability $S=-1$ can be sustained. This is consistent with the upper bound on momentum transport in turbulent Couette flow derived by Busse [10]. He found that no state of turbulent motion can exist for

$$4Re \leq \frac{1708}{4ReRo} + 4ReRo. \tag{4.3}$$

This criterion for turbulence to exist can be recast into an explicit constraint on the rotation number:

$$Ro < \frac{1}{2}\left(1 + \sqrt{1 - 4\frac{1708}{16}\frac{1}{Re^2}}\right). \tag{4.4}$$

For $Re = 1300$, this formulae suggests that turbulence can be maintained only if $Ro < 0.9999$, i.e., fully consistent with our intuition-based conjecture that Ro cannot exceed unity. The recent flow visualizations of Alfredsson and Tillmark [1] indeed showed that the turbulence was suppressed and the flow relaminarized for rotation numbers beyond 1.0.

The partition between viscous and turbulent shear stresses is shown in Fig. 5. Due to the substantial linear portion of the mean velocity profile in Fig. 4, the viscous shear stress is constant over the entire center region and the stress magnitude is 3-4 times larger
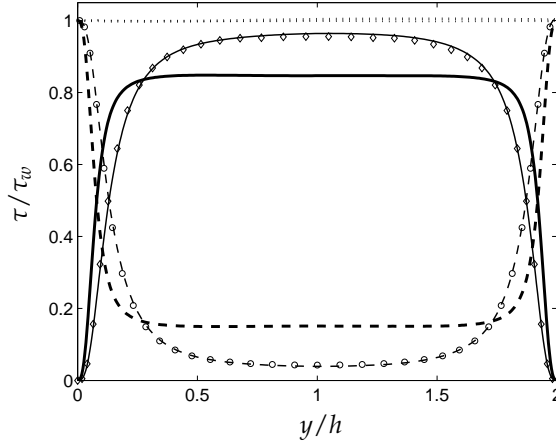
Figure 5: Variation of viscous and turbulent shear stress across the flow for $Ro=0.7$ (bold lines) compared with the corresponding data for non-rotating Couette flow (thin lines) and DNS data from [8] for $Ro=0$ (symbols). Viscous shear stress $\mu(dU/dy)/\tau_w$ ($---$; $\circ$) and turbulent shear stress $-\rho\overline{uv}/\tau_w$ (——; $\diamond$).

than in the non-rotating case. Let us recall that the viscous shear stress $\mu dU/dy$, when normalized by τ_w, is equal to dU^+/dy^+, i.e., the inner-variable mean shear rate. The slope of the mean velocity in outer variables, as in Fig. 4, is related to dU^+/dy^+ in Fig. 5 in accordance with:

$$\frac{d\widetilde{U}}{d\widetilde{y}} \equiv \frac{d(U/2U_w)}{d(y/h)}) = \frac{1}{2}Re^{-1}Re_\tau^2\frac{dU^+}{dy^+}. \tag{4.5}$$

The local vorticity ratio S can be deduced from either of the two, i.e.,

$$S = -\frac{2\Omega^F}{dU/dy} = -\frac{1}{2}Ro\left(\frac{d\widetilde{U}}{d\widetilde{y}}\right)^{-1} = -RoReRe_\tau^{-2}\left(\frac{dU^+}{dy^+}\right)^{-1}. \tag{4.6}$$

With dU^+/dy^+ approximately equal to 0.16 over nearly 80% of the cross-section in Fig. 5, the core region value of $S \approx -1.004$. In the substantial part of the cross-section where S is practically equal to -1.0, the absolute mean vorticity vanishes and the shear-Coriolis instability is neutral. A further elaboration on the consequences of this observation is postponed until Section 5.

The constancy of the total mean shear stress, as expressed in Eq. (2.4), therefore also makes the turbulent shear stress $-\rho\overline{uv}$ constant over about 80% of the cross section. The turbulent shear stress equals the viscous shear stress at about $y/h \approx 0.07$, which is significantly closer to the wall than in the non-rotating case where the two shear stresses equal at $y/h \approx 0.10$. This intersection point is exactly where the turbulent energy production attains its maximum value (see the discussion in Section 2.2). This observation therefore reflects that the imposition of rotation makes the near-wall layers thinner.

This suggestion is confirmed by the profiles of the turbulence intensities in Fig. 6(a), which show that the peak positions are indeed closer to the walls than for $Ro=0$. An even
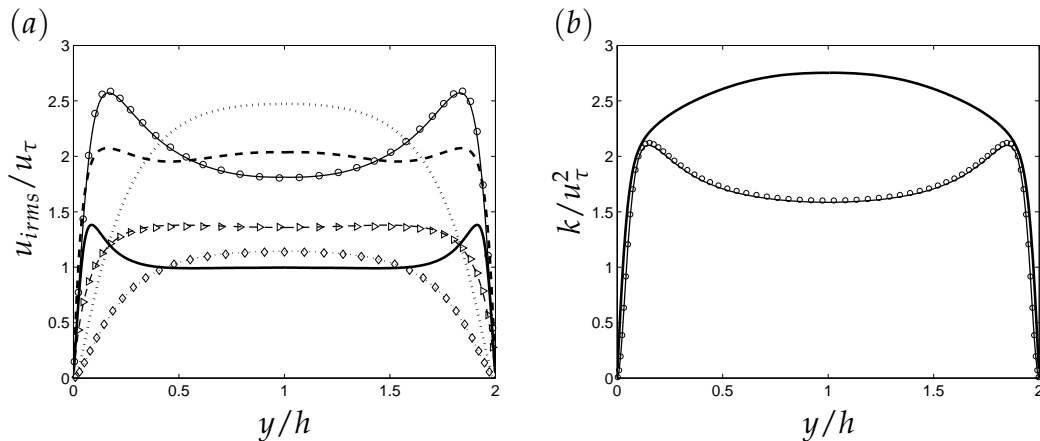
Figure 6: Variation of turbulence intensities and kinetic energy k across the flow for $Ro = 0.7$ (bold lines) and $Ro = 0$ (thin lines) compared with the corresponding data for non-rotating Couette flow (symbols) from [8]. The results are scaled with the corresponding friction velocities. (a) Turbulence intensities u_{rms} (——; ○), v_{rms} (···; ◇), w_{rms} (– – –; ▷); (b) Turbulent kinetic energy k for $Ro = 0.7$ (bold line) and $Ro = 0$ (thin line) compared with DNS data (○) from [8].

more striking observation is the reversal of the conventional anisotropy $u_{rms} > w_{rms} > v_{rms}$ in wall turbulence in general and in non-rotating Couette flow in particular. In the rapidly rotating Couette flow $v_{rms} > w_{rms} > u_{rms}$ over a substantial part of the flow. While the wall-normal velocity fluctuations v_{rms} are consistently smaller than the other velocity fluctuations for $Ro = 0$, v_{rms} exceeds the streamwise fluctuations u_{rms} over the central 80% of the cross section and the spanwise fluctuations w_{rms} over more than 60% of the flow.

The dominance of the wall-normal velocity fluctuations affects the distribution of the mean turbulent kinetic energy k across the flow as shown in Fig. 6(b). The conventional near-wall peaks are totally absent and the maximum value of k is observed midway between the walls where also v_{rms} attains its maximum. The energy level is higher over the entire core region and exceeds that of the non-rotating flow with about 75% at the center. The simultaneous observations of a higher turbulence level and reduced flow resistance can only be understood if the rotating turbulence is less efficient in wall-normal mixing (i.e., shear production) than conventional wall turbulence.

In spite of the above observation that the wall-normal fluctuations dominate over the streamwise fluctuations, the outcome of a quadrant analysis shown in Fig. 7 does not show any qualitative differences brought about by the system rotation. In both cases, the fourth quadrant ($Q4$-events) dominates very close to the wall whereas contributions from the second quadrant ($Q2$) are more influential further out. It is readily seen, however, that the position at which the two kind of events are of equal importance has shifted from $y^+ \approx 14$ in the non-rotating case to about $y^+ \approx 6$ for $Ro = 0.7$. It can also be noticed that the adverse contributions from the $Q1$ and $Q3$ events have been significantly reduced, especially near the wall. Although the $Q4$-dominance over the $Q2$-events still persists in the vicinity of the wall, the relative contribution from the $Q4$-events has been substantially
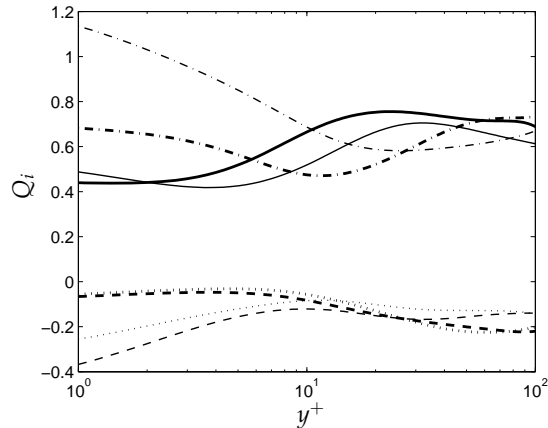
Figure 7: Fractional contributions to the turbulent shear stress $-\overline{uv}$ from the four quadrants. Data from the rotating Couette flow (bold lines) compared with the non-rotating case (thin lines). $(- - -)$ $Q1(u>0,v>0)$; (———) $Q2(u<0,v>0)$; $(\cdots)$ $Q3(u<0,v<0)$; $(- \cdot -)$ $Q4(u>0,v<0)$.

reduced, thereby suggesting that the importance of the sweep events has diminished. It is noteworthy that a similar reduction of the fractional contribution of sweeping events relative to ejections was observed also at the anti-cyclonic side of the rotating Poiseuille flow both in the computer experiments by Kristoffersen and Andersson [22] and the laboratory experiments by Nakabayashi and Kitoh [31]. In that flow, however, the turbulent shear stress $-\rho\overline{uv}$ was increased due to the imposed system rotation, whereas the shear stress is lowered in the present flow. A particular feature of Couette flow turbulence is that an ejection ($Q2$-event) from the fixed wall appears as a sweeping event ($Q4$) when seen from the moving wall and vice versa.

For the sake of completeness, the skewness S and flatness F of the fluctuating velocity components are shown in Fig. 8. The skewness of u is positive in the core region and inevitably goes to zero at the center due to symmetry. This contrasts with the non-rotating case in which $S(u)$ is negative in the core. The latter is generally ascribed to the dominance of outbursts or ejections beyond $y^+ \approx 12$ whereas so-called sweeps are the major contributor to the turbulence production in the vicinity of the wall. The positive value of $S(u)$ in the core region of the rotating Couette flow must therefore imply that the conventional stress-producing mechanism has been suppressed. The flatness of u is substantially higher than 3.0 in the core region which suggests more frequent occurrences of extreme events than in a Gaussian distribution.

The skewness and flatness of the wall-normal velocity component v become roughly constant, i.e., $S(v) \approx 0$ and $F(v) \approx 2.8$, in the core region. In the immediate vicinity of the wall, the skewness of v has become negative with the wall-value $S(v) \approx -1$ rather than being close to zero as in the non-rotating case. This implies that extreme wall-ward motions, although possibly rare, are more frequent than extreme out-rushs. The violent wall-ward motions may furthermore be correlated with strong positive streamwise fluctuations and thus contribute to the Reynolds shear stress. This is in contrast with other wall-flows,
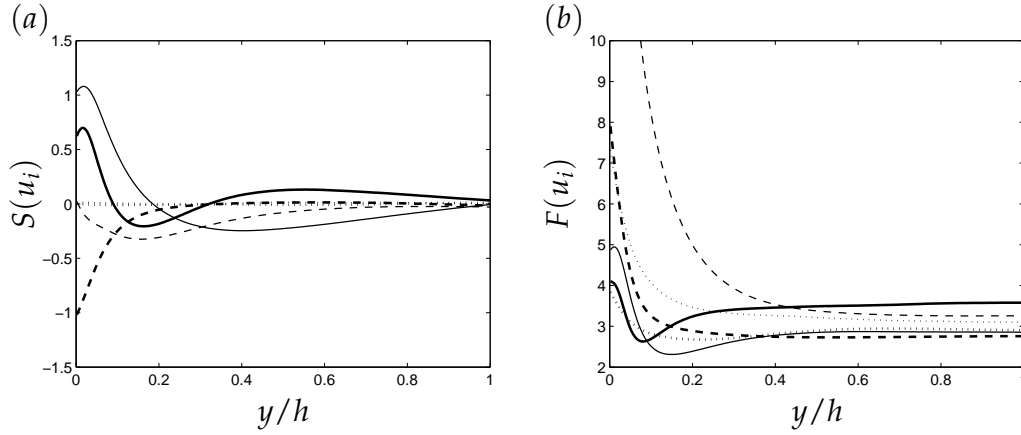
Figure 8: Higher-order moments of the velocity fluctuations u_i. (a) Skewness $S(u_i)$; (b) Flatness $F(u_i)$. Data from the rotating Couette flow (bold lines) compared with the non-rotating case (thin lines). (——) u; (– – –) v; ($\cdots$) w.

notably plane Poiseuillle flow, where both $S(u)$ and $S(v)$ are positive in the vicinity of the wall and extreme u-motions are therefore not correlated with large v-motions.

The symmetry properties of the present flow imply that $S(w)\!=\!0$. The skewness of w, as deduced from the simulated flow field, is essentially zero both in the rotating and non-rotating case and thereby confirms the adequacy of the sampling.

5   Energy considerations and Reynolds-stress budgets

The budgets of the individual components of the Reynolds stress tensor provide insight into the interactions between the large-scale turbulence and the mean flow. The budgets of the three diagonal components and the only non-zero off-diagonal Reynolds stress component are shown in Fig. 9.

In order to assist in the interpretation of the budgets, it might be helpful to consider the production terms due to mean shear and rotation. For unidirectional mean flow $U(y)$ rotating about the z-axis, we obtain:

$$P_{xx}+G_{xx}=-2\overline{uv}\frac{dU}{dy}+4\Omega^F\overline{uv}=(1+S)P_{xx}\approx 0, \tag{5.1a}$$

$$P_{yy}+G_{yy}=0-4\Omega^F\overline{uv}=-SP_{xx}\approx P_{xx}, \tag{5.1b}$$

$$P_{xy}+G_{xy}=-\overline{v^2}\frac{dU}{dy}-2\Omega^F(\overline{u^2}-\overline{v^2})=\left[1+S\left(1-\frac{\overline{u^2}}{\overline{v^2}}\right)\right]P_{xy}\approx\frac{\overline{u^2}}{\overline{v^2}}P_{xy}=-\overline{u^2}\frac{dU}{dy}. \tag{5.1c}$$

Here, the rightmost part of the each of the above equations is valid only for $S\!\approx\!-1.0$. Data for the individual production terms in the core region, together with the pressure-strain rates and the dissipation rates, are provided in Table 1.
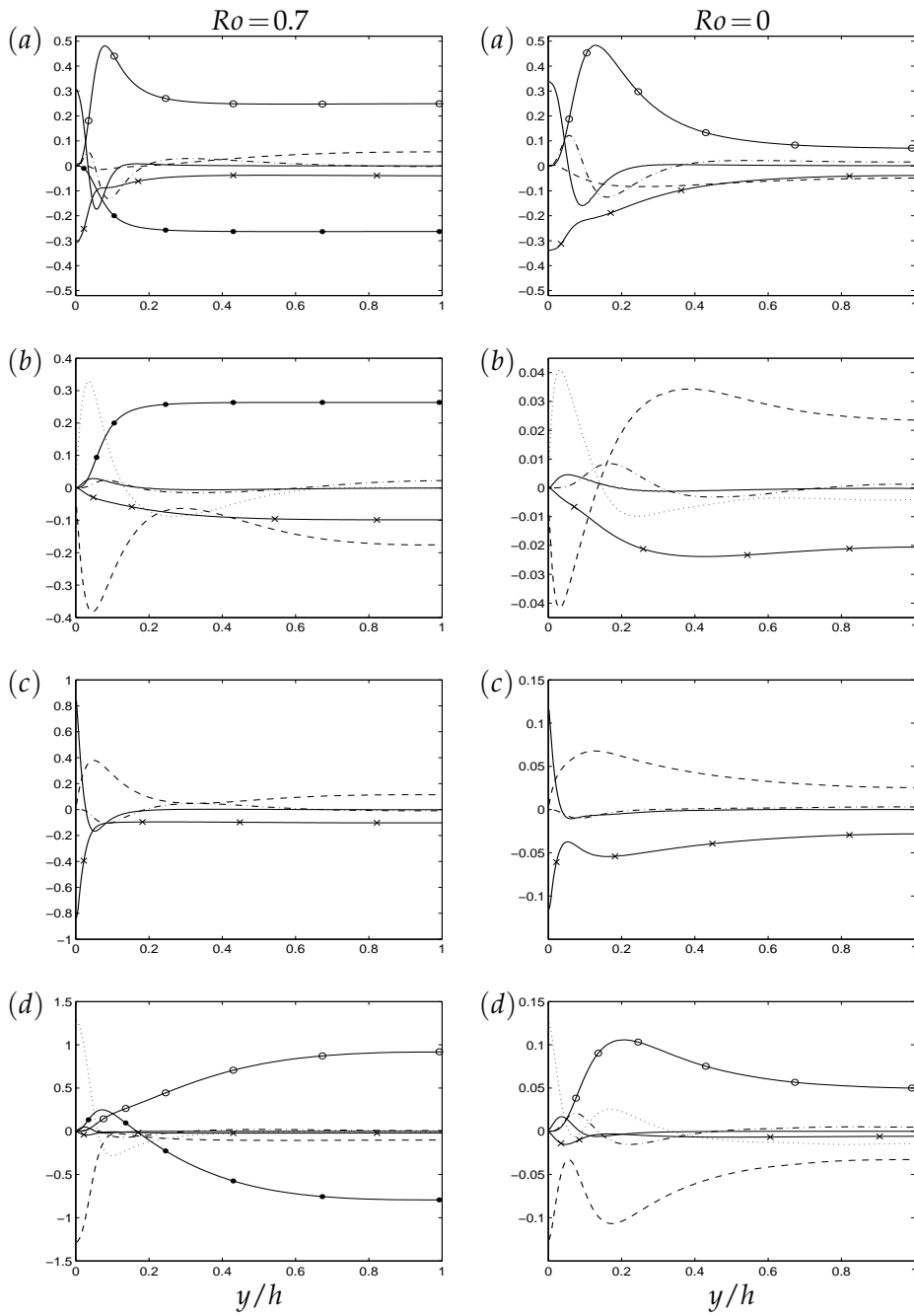
Figure 9: Budgets of the individual Reynolds stress components. The terms are scaled with u_τ^4/ν. Note the difference between the tick-marks along the ordinate axis. (a) uu; (b) vv; (c) ww; (d) $-uv$. (—o—) P_{ij}; (—•—) G_{ij}; (− · −) D_{ij}^T; (· · ·) D_{ij}^P; (——) D_{ij}^V; (− − −) Π_{ij}; (—✕—) $-\varepsilon_{ij}$.

Table 1: Core-region values of the leading terms in the second-moment budgets evaluated at the symmetry plane $y/h=1.0$ for $Ro=0.7$. All terms are scaled with u_τ^4/ν. The imbalance refers to the sum of the leading terms that are included in the table.

	$i=1,j=1$	$i=2,j=2$	$i=3,j=3$	$i=1,j=2$
P_{ij}	$+0.249$	————	————	-0.919
G_{ij}	-0.264	$+0.264$	————	$+0.794$
Π_{ij}	$+0.056$	-0.176	$+0.114$	$+0.102$
$-\varepsilon_{ij}$	-0.040	-0.099	-0.103	$+0.021$
Imbalance	$+0.001$	-0.011	$+0.011$	-0.002

It is well known that the mean shear only contributes to streamwise velocity fluctuations. The system rotation introduces source terms both in the streamwise and wall-normal directions, whereas the fluctuations in the direction of the axis of rotation are unaffected. It is particularly noteworthy that the rotational terms in Eq. (5.1) cancel out if the second-moment equation (2.5) is contracted to give an equation for the turbulent kinetic energy. This is intuitively evident since the instantaneous Coriolis force always acts perpendicular to the instantaneous velocity vector. The Coriolis force can therefore neither produce work nor directly alter the energy of the flow. The substantially higher mean turbulent kinetic energy in the rotating case (see Fig. 6(*b*)) must therefore be ascribed to indirect effects of system rotation. The weakly and moderately rotating Couette flow considered by Bech and Andersson [6,7] was affected by large-scale counter-rotating roll cells, as was the rotating Poiseuille flow studied by Johnston *et al.* [20] and Kristoffersen and Andersson [22] and others. Such roll cells contribute substantially to the kinetic energy of the flow, whereas the present Couette flow is free of rotational-induced large-scale vortices. The excess kinetic energy level can therefore only be a result of an indirect influence of the Coriolis force on the turbulence structure.

The anisotropy and inhomogeneity of a turbulent flow field is caused by the production terms in Eq. (2.5). In the orthogonally rotating Couette flow, the only non-zero production terms are those given in Eq. (5.1) above. In non-rotating channel and Couette flow, the turbulence is produced by mean shear, i.e., $P_{xx}>0$, whereas P_{yy} and P_{zz} both are zero.

Throughout the core region of the rapidly rotating Couette flow $S\approx-1$. This implies that the rotational turbulence production G_{xx} just outweighs the conventional mean shear production P_{xx} (see Fig. 9(*a*)) with the crucial implication that no energy is transferred from the mean flow into the streamwise velocity fluctuations. Instead, the correlation between the wall-normal Coriolis force and the wall-normal velocity fluctuations in Eq. (5.1b) becomes a significant source of $\overline{v^2}$, as seen in Fig. 9(*b*).

As far as the shear stress $-\rho\overline{uv}$ is concerned, the rotational production G_{xy} assists the mean shear production P_{xy} as long as the conventional shear flow anisotropy $\overline{u^2}>\overline{v^2}$ persists. In the presence of an abnormal anisotropy $\overline{v^2}>\overline{u^2}$, however, the situation is reversed and G_{xy} tends to reduce the turbulent shear stress, as can be observed from the budget

for $-\rho\overline{uv}$ in Fig. 9(d). The overall implication is that the streamwise velocity fluctuations have taken over the role played by wall-normal fluctuations for $Ro\!=\!0$, as demonstrated by Eq. (5.1c). It is noteworthy, however, that what is left in (5.1c) stems from interactions between streamwise velocity fluctuations and the wall-normal component of the instantaneous Coriolis force.

The rightmost parts of Eq. (5.1) apply in the core region of the rapidly rotating Couette flow where $S\!\approx\!-1.0$. In this region turbulent velocity fluctuations are contributed into the wall-normal direction by the action of the Coriolis force whereas no turbulence is produced in the streamwise and spanwise directions. Thus, in order for turbulence to prevail, a redistribution mechanism is required which transfers turbulent energy from the wall-normal direction into the two other coordinate directions. If no energy is fed into the streamwise direction, the correlation $\overline{uv}$ required for the turbulence production (5.1b) will vanish and the turbulence will eventually fade away. It is therefore speculated that the quenching of the turbulence in rapidly rotating Couette flow reported by Bech and Andersson [7] and Alfredsson and Tillmark [1] results from the attenuation of the crucial transfer mechanism between the directional components of the instantaneous velocity vector.

Outside of the core region, however, the local vorticity ratio S increases monotonically from -1 to -0.16 at the walls. Here, the wall-value of S is readily obtained from Eq. (4.6) with $dU^+/dy^+\!=\!1.0$. The simplifications introduced in the rightmost parts of Eq. (5.1) do no longer apply, which for instance implies that streamwise velocity fluctuations produced by mean shear are only partially hampered by the rotational sink term near the walls, see, e.g., Fig. 9(a).

The preceding discussion is valid only if the rotation is sufficiently fast, i.e., beyond the supercritical regime in which roll cells co-exist with the turbulence. The existence of a purely turbulent flow regime for anti-cyclonic rotation rates Ro above 0.5 and a roll-cell dominated regime for $0 < Ro < 0.5$ [6, 7] is analogous to the existence of two different flow regimes in the Taylor-Couette flow recently addressed by Dubrulle *et al.* [12]. The two conceptually different turbulent regimes for anti-cyclonic rotation contrast with the existence of only one turbulent flow regime in plane Couette flow subjected to cyclonic rotation.

6 Vorticity dynamics

The vorticity is an essential kinematic property of fluid motion, as illustrated by the snapshots of the flow field shown in Fig. 10. In order to focus on the streamwise vorticity, the instantaneous λ_2-field (to be defined in Section 6.2) has been pre-multiplied by ω_x before the iso-contours were plotted. It is evident from these plots that the streamwise vorticity has been substantially enhanced when the flow is subjected to strong anti-cyclonic rotation as in Fig. 10(b). Furthermore, we consider the distribution of $\theta\!=\!tan^{-1}(\omega_y/\omega_x)$, the inclination angle of the projection on the (x,y)-plane of the vorticity vector. Fig. 11 shows
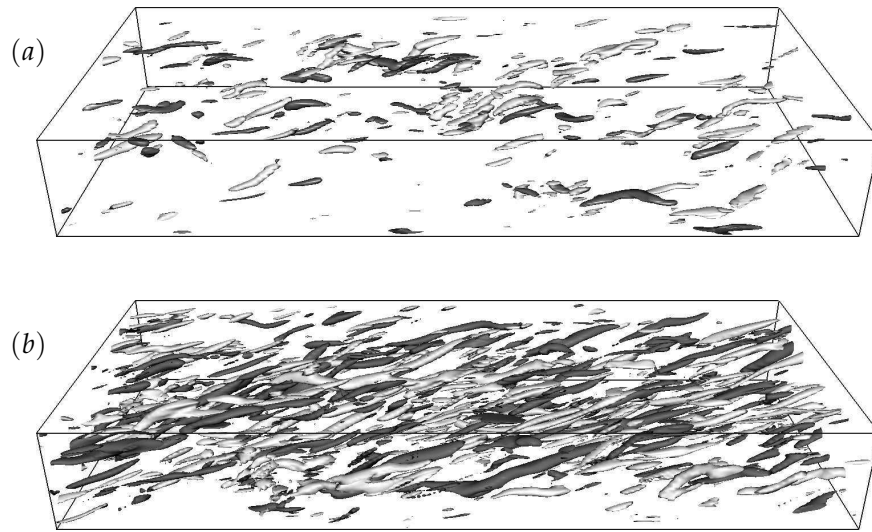
(a)

(b)

Figure 10: Instantaneous flow field visualised by means of iso-contours of $-\lambda_2\omega_x$. (a) $Ro=0$; (b) $Ro=0.7$. The contour level is the same in both parts of the figure. Positive and negative contour levels are distinguished by light and dark shading, respectively.
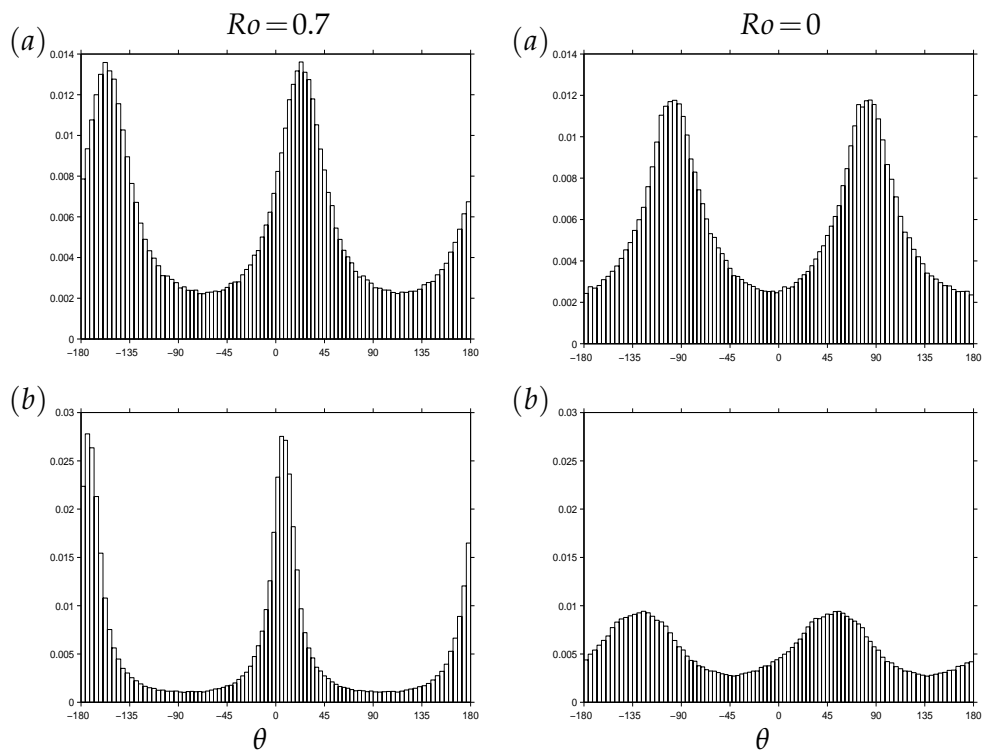
(a) $Ro=0.7$

(a) $Ro=0$

(b)

(b)

Figure 11: Probability distribution of the inclination angle θ. (a) $y^+=10$; (b) $y^+=50$.

the inclination angle θ close ($y^+=10$) and far away ($y^+=50$) from the wall for both rotating and non-rotating cases. The results indicate a distinct effect of system rotation on the flow structures not only in the core region ($\theta\approx10$) but even in the flow region close to the wall ($\theta\approx25$). These observations will be examined by means of vorticity statistics in the following subsections.

6.1 Mean vorticity and mean Lamb vector

It is evident from the mean velocity profile in Fig. 4 and the partition between viscous and turbulent shear stress components in Fig. 5 that the mean vorticity $\Omega_z=-dU/dy$ is constant and roughly equal to the background vorticity $2\Omega^F$ over about 80% of the cross-section. The integrated equation for the mean vorticity (2.8) is valid over the entire flow region. The constancy of Ω_z in the core region makes the viscous term in (2.8) vanish and leaves a balance between $\overline{w\omega_y}$ and $-\overline{v\omega_z}$. Such velocity-vorticity correlations are associated with the Lamb vector:

$$\boldsymbol{\lambda}=\boldsymbol{u}\times\boldsymbol{\omega}. \tag{6.1}$$

The above definition of the instantaneous Lamb vector is the same as that adopted by Orlandi [32] and Liu and Lu [26] while Moffatt and Tsinober [29] used the definition $\boldsymbol{\omega}\times\boldsymbol{u}$. The mean value $\boldsymbol{\Lambda}$ of the instantaneous Lamb vector $\boldsymbol{\lambda}$ lies entirely in the (x,y)-plane, i.e., $\Lambda_z=0$, due to symmetries. The two non-zero components are in the present case:

$$\Lambda_x=\overline{v\omega_z}-\overline{w\omega_y} \quad \text{and} \quad \Lambda_y=-U\Omega_z+\overline{w\omega_x}-\overline{u\omega_z}. \tag{6.2}$$

Here, the velocity-vorticity correlations which contribute to the streamwise component are recognized as the two first contributions to the integrated mean vorticity balance (2.8) which therefore can be stated as $\Lambda_x=\nu d\Omega_z/dy$. The mean vorticity Ω_z, which is negative across the entire flow, increases monotonically from its minimum value at $y=0$ to its maximum (but still negative) level in the core. The resulting $d\Omega_z/dy>0$ in the near-wall region is balanced by $-\Lambda_x$ in accordance with Eq. (2.8); see Fig. 12. The major contribution to the positive Λ_x in the near-wall region stems from the negative correlation between the spanwise velocity fluctuations and the wall-normal vorticity. It is noteworthy that Λ_x is roughly doubled in the presence of system rotation in the vicinity of the walls. This increase in the Lamb vector is in qualitative agreement with the rotating Poiseuille flow simulations by Liu and Lu [26]. They reported a substantial enhancement of Λ_x near the pressure (i.e., anti-cyclonic) side of their rotating channel, whereas Λ_x was nearly suppressed near the suction (i.e., cyclonic) side.

In the core region of the Couette flow where the mean vorticity is uniform, $d\Omega_z/dy\approx0$ and the streamwise component of the mean Lamb vector vanishes, i.e., $\overline{v\omega_z}\approx\overline{w\omega_y}$. It is noteworthy from Fig. 12 that Λ_x is suppressed already at $y\approx0.3h$ in the presence of system rotation. Since the Lamb vector is responsible for the energy cascade, this observation implies that the energy transfer from large to small scales is inhibited by the imposed rotation.
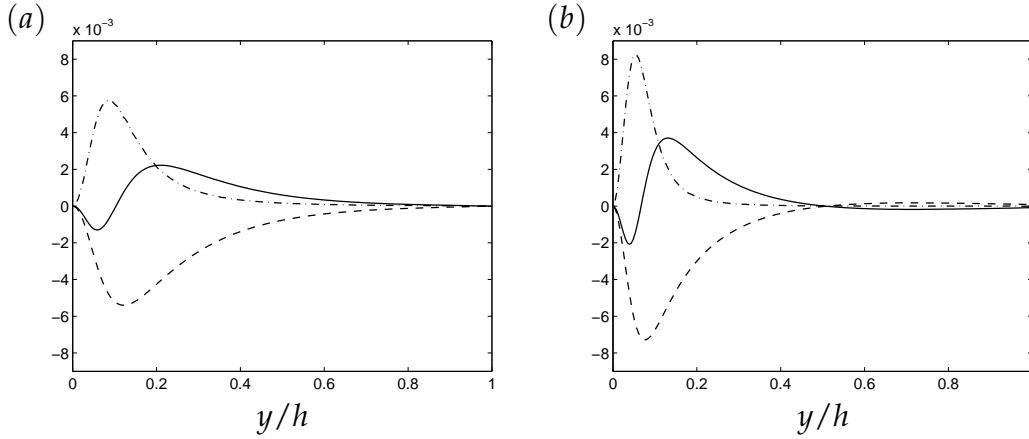
Figure 12: Individual terms (———) $\overline{w\omega_y}$; $(- - -)$ $-\overline{v\omega_z}$; and $(- \cdot -)$ $\nu d\Omega_z/dy$ in the integrated mean vorticity equation (2.8). Notice that the sum $\overline{v\omega_z} - \overline{w\omega_y}$ equals Λ_x, i.e., the x-component of the mean Lamb vector in Eq. (6.2). (a) Non-rotating Couette flow; and (b) Anti-cyclonically rotating Couette flow with $Ro=0.7$.

The role of the mean Lamb vector in the turbulence productions is readily revealed if the production of turbulent kinetic energy by mean shear in Eq. (2.6) is rewritten as:

$$P_K = \frac{1}{2}P_{ii} = -\overline{u_iu_k}\frac{\partial U_i}{\partial x_k} = -\varepsilon_{ijk}\overline{\omega_ju_i}U_k - \frac{\partial \overline{u_iu_k}U_k}{\partial x_i} = -\Lambda_xU - \frac{dU\overline{uv}}{dy}. \tag{6.3}$$

Here, $\varepsilon_{ijk}\overline{\omega_ju_i}$ comprises the velocity-vorticity correlations involved in the k-component of the mean Lamb vector. The rightmost part of Eq. (6.3) shows that only the streamwise component of Λ contributes to the turbulent energy production in this particular flow. In the core region where the shear stress $-\overline{uv}$ remains constant and Λ_x vanishes, the more conventional expression (2.6) for the kinetic energy production is recovered. It can readily be inferred from the data in Fig. 12 that the consistently positive value of Λ_x is responsible for a loss of turbulent energy, i.e., transfer from large to small scales and ultimately dissipation. This loss is, however, more than outweighed by advection of large-scale energy.

The helicity density is defined as

$$h = \boldsymbol{u} \cdot \boldsymbol{\omega}. \tag{6.4}$$

The helicity h is related to the Lamb vector through the mathematical vector identity [34]:

$$h^2 + \lambda^2 = |\boldsymbol{u} \cdot \boldsymbol{\omega}|^2 + |\boldsymbol{u} \times \boldsymbol{\omega}|^2 = |\boldsymbol{u}|^2|\boldsymbol{\omega}|^2. \tag{6.5}$$

According to (6.4) helicity is a measure of the degree of alignment of the vorticity vector and the velocity vector. High levels of helicity are believed to hamper the energy cascade and therefore also the energy dissipation. In the present flow, however, the mean value of the helicity density defined in (6.4) vanishes identically due to the inherent symmetries associated with the statistical homogeneity in the spanwise direction.
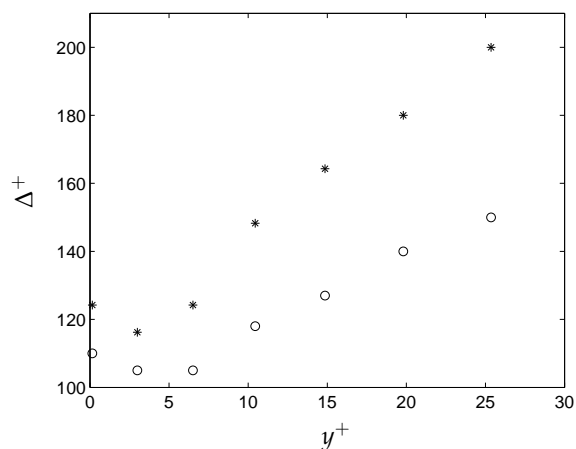
Figure 13: Variation of the mean streak spacing $\Delta^+ = \Delta \cdot u_\tau / \nu$ in the near-wall region for rotating ($*$) and non-rotating ($\circ$) Couette flow.

6.2   Near-wall streaks and coherent flow structures

The wall-region of a non-rotating plane Couette flow resembles that in other simple wall-bounded flows, e.g. the plane Poiseuille flow. The presence of elongated streamwise streaks with a typical mean spacing Δ of about 100 wall units (i.e., ν/u_τ) are among the most characteristic features of wall turbulence. The particular spanwise separation which corresponds to the distinct minimum of the two-point correlation of u in Fig. 3 is a measure of the mean separation between low- and high-speed motions. The mean streak spacing Δ is estimated as twice this distance. The results in Fig. 13 show that Δ^+ increases nearly linearly with the wall distance from about 100 in the immediate vicinity of the wall to about 150 at $y^+ = 30$ in the absence of rotation, i.e., just as in the non-rotating Poiseuille flow. In the presence of system rotation, a somewhat larger streak spacing Δ^+ is observed. This is opposite to the distinctly reduced streak spacing observed at the anti-cyclonic (pressure) side of the rotating Poiseuille flow considered by Kristoffersen and Andersson [22]. The enhanced streak density in that study was accompanied by a higher wall-friction velocity. In the present case, on the other hand, the increased streak separation is associated with a reduction in u_τ, i.e., fully consistent with the widely accepted belief that the streak density is closely related to the wall friction.

An efficient scalar quantity frequently used to identify regions of localized vortices in a flow field is λ_2 introduced by Jeong and Hussain [18] as the second largest eigenvalue of the tensor $s_{ik}s_{kj} + r_{ik}r_{kj}$ where s_{ij} and r_{ij} are the strain-rate and rotation-rate tensors, respectively. The distribution of the *rms*-value of λ_2 from the wall and towards the center is shown in Fig. 14. λ_{2rms} is normalized by u_τ^4/ν^2, i.e., the reciprocal of the viscous time scale ν/u_τ^2 squared. In the absence of rotation, the near-wall variation closely resembles that of plane Poiseuille flow with a peak located at about $y/h \approx 0.2$ or $y^+ \approx 16$. The peak level is, however, more than 50% higher in the Couette flow than in the Poiseiulle
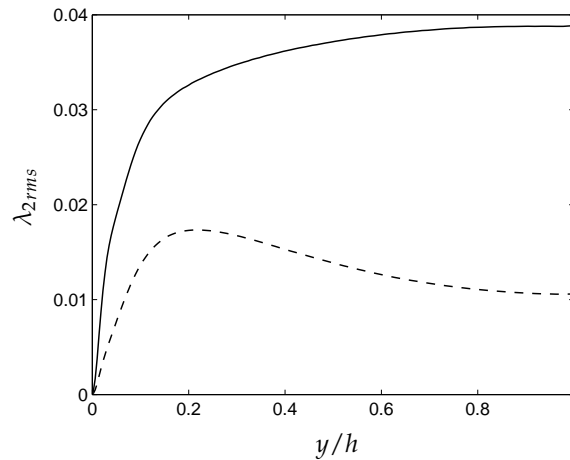
Figure 14: Variation of λ_{2rms} from the wall to the centerline for the rotating (solid line) and non-rotating (broken line) Couette flow. The data are scaled with u_τ^4/ν^2.

flow and the reduction of λ_{2rms} towards the centerline is by far more modest than in the channel flow. When the Couette flow is subjected to rapid anti-cyclonic rotation, however, λ_{2rms} increases monotonically all the way from the wall towards the center and the λ_2-level at the centerline is more than 3 times higher than without rotation. This is yet another manifestation of the anomaly of the flow dynamics in the core region.

6.3 Enstrophy and vorticity budgets

The root-mean-square values of the fluctuating vorticity components are shown in Fig. 15. The only resemblance with conventional wall-flow behaviour is that the wall-normal vorticity goes to zero at the wall simply as a result of the no-slip condition. While spanwise vorticity fluctuations $\overline{\omega_z^2}$ normally dominate in the near-wall region, see, e.g., Antonia and Kim [3], the streamwise vorticity $\overline{\omega_x^2}$ is by far more intense in the present case. This enhancement due to system rotation overshadows the characteristic near-wall peak of $\overline{\omega_x^2}$ which can be observed for $Ro=0$. This peak has usually been associated with the presence of coherent streamwise-oriented vortices. A striking homogeneity of the fluctuating vorticity field is observed in the entire core region. Here, a distinct and anomalous anisotropy prevails with the streamwise vorticity fluctuations exceeding the two other components, which on the other hand turn out to be practically equal and thus reflects an axisymmetry of the vorticity field. This contrasts with the non-rotating case in which the vorticity field is close to an isotropic state in the core region.

Following Antonia and Kim [3], the behaviour of the individual vorticity components can be further explored by examining the dominating terms in the second-moment equation (2.9). They based their analysis on their equation (14) which appears as an equation for twice the scalar enstrophy due to the implicit summation over repeated indices i and
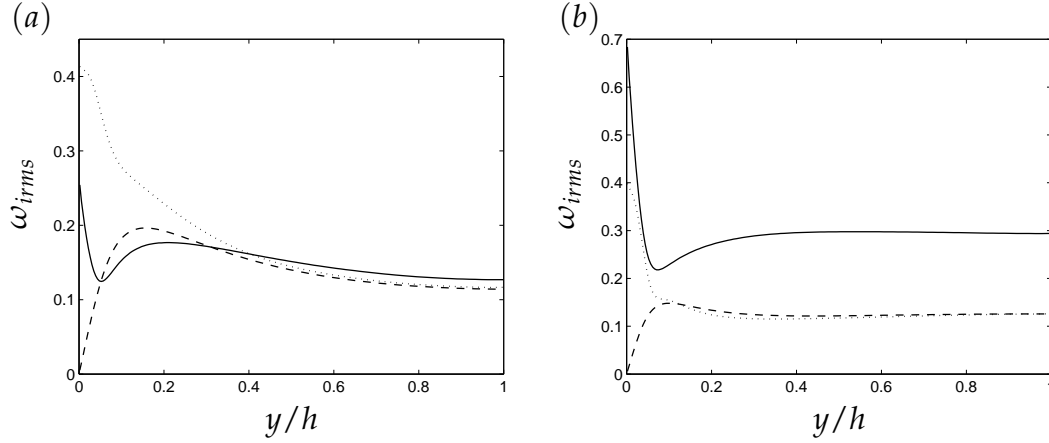
Figure 15: Root-mean-square vorticity fluctuations normalized by u_τ^2/ν. (a) Non-rotating Couette flow; and (b) Anti-cyclonically rotating Couette flow with $Ro=0.7$. (——) $\omega_{x_{rms}}$; (– – –) $\omega_{y_{rms}}$; (···) $\omega_{z_{rms}}$.

j. Their equation (14) is consistent with the diagonal elements of present equation (2.9) for the individual second-moments provided that summation is only carried out for j whereas the conventional summation rule is not applied for the repeated index i which rather should be taken as either 1, 2 or 3. In the present context, the stretching term $S5_{ij}$ is of particular concern. Tennekes and Lumley [36] referred to this term as a mixed production term. This term plays a major role in the viscous sublayer in channel flows [3] where it peaks about $y^+\approx 4$. In a rotating frame-of-reference, this is the only term in the second-moment vorticity budgets that explicitly includes the system rotation; see Eq. (A.13) in the Appendix.

Table 2: Core-region values of the leading terms in the second-moment vorticity budgets evaluated at the symmetry plane $y/h=1.0$ for $Ro=0.7$. All terms are scaled with $(u_\tau^2/\nu)^3$. The imbalance refers to the sum of the leading terms that are included in the table.

	$i=j=1$	$i=j=2$	$i=j=3$	Enstrophy
$S3_{ij}\cdot 10^3$	− 0.01	+ 1.26	+ 1.90	+ 1.58
$S4_{ij}\cdot 10^3$	+ 6.60	———	———	+ 3.30
$S5_{ij}^{I}\cdot 10^3$	− 3.20	+ 3.32	− 0.10	+ 0.01
$S5_{ij}^{II}\cdot 10^3$	+ 3.20	− 3.34	+ 0.10	− 0.02
$V7_{ij}\cdot 10^3$	− 6.50	− 1.34	− 1.88	− 4.86
Imbalance $\cdot 10^3$	+ 0.09	− 0.10	+ 0.02	+ 0.01

The vorticity budgets presented in Fig. 16 show that most of the terms in (2.9) contribute in the near-wall region, whereas a major simplification is observed further away from the walls. Several terms become of negligible importance in the core region and those that contribute remain constant over at least 60% of the cross-section (see Table 2). The budget of the spanwise vorticity in Fig. 16(c), for instance, simplifies to a balance
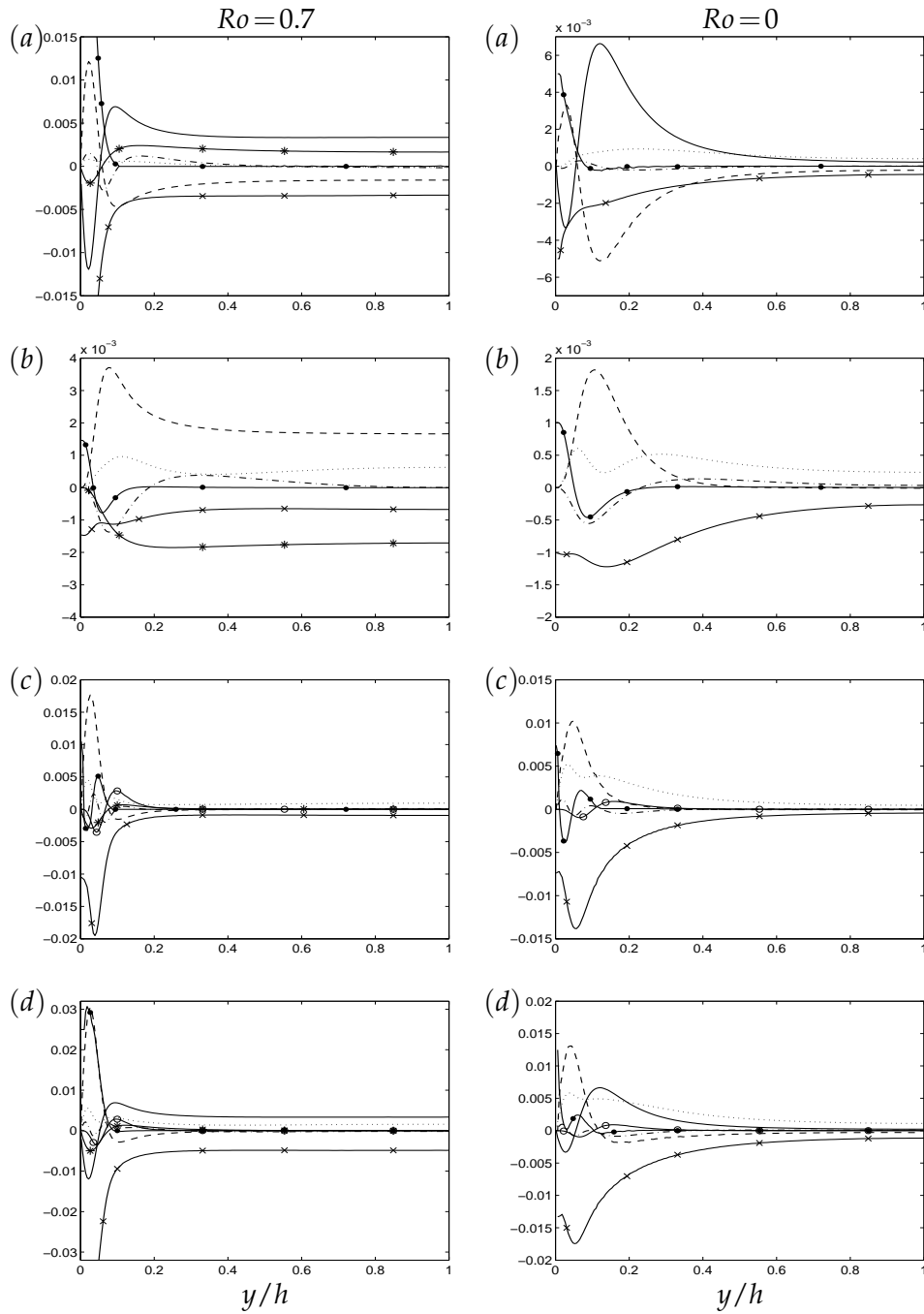
Figure 16: Budgets of (a) $\frac{1}{2}\overline{\omega_x^2}$, (b) $\frac{1}{2}\overline{\omega_y^2}$, (c) $\frac{1}{2}\overline{\omega_z^2}$ and (d) enstrophy $\frac{1}{2}\overline{\omega_i\omega_i}$. The individual terms are scaled with $(u_\tau^2/\nu)^3$. (—○—) $T1_{ij}$; (– · –) $T2_{ij}$; (· · ·) $S3_{ij}$; (——) $S4_{ij}$; (– – –) $S5_{ij}^I$; (—*—) $S5_{ij}^{II}$; (—●—) $V6_{ij}$; (—×—) $V7_{ij}$.

between stretching by fluctuating velocity gradients $S3_{zz}$ and viscous dissipation $V7_{zz}$. Such a balance prevails also in the central part of the plane channel flow examined by Antonia and Kim [3].

Most of the terms in the $\overline{\omega_y^2}$-budget are vanishingly small in the absence of rotation, in particular in the core region. It is noteworthy that the present budget in Fig. 16(b) is rather different from the corresponding Poiseuille flow budget provided by Antonia and Kim [3] in their Fig. 8(b). They observed that two stretching terms $S4$ and $S5$ are the dominating sources of wall-normal vorticity fluctuations. In the present case, however, $S4_{yy}$ is absent as it should be for symmetry reasons. In fact, $S4$ contributes only to streamwise vorticity fluctuations in unidirectional shear flows. With system rotation imposed, the important stretching term $S5_{yy}$ associated with the mean flow vorticity is outweighed by the stretching due to the imposed rotation in the entire core region. This leaves a balance between turbulent vortex stretching of vorticity fluctuations $S3_{yy}$ and viscous dissipation $V7_{yy}$, i.e., similarly as in the spanwise direction.

The streamwise vorticity fluctuations are the main contributor to the enstrophy $\frac{1}{2}\overline{\omega_i\omega_i}$ in the rapidly rotating Couette flow. According to the budget in Fig. 16(a), $S3_{xx}$ is reduced with rotation whereas $S4_{xx}$ is increased. Again, the stretching due to mean flow vorticity exactly balances the stretching due to rotation and thereby leaves a balance between the $S4_{xx}$ and $V7_{xx}$ in the core region. This contrasts with the non-rotating case in which $S3_{xx}$ is the major source term.

The enstrophy balance is readily obtained as the trace of Eq. (2.9), i.e., as the sum of the diagonal terms of the individual second-moments of the vorticity fluctuations. Let us recall from Section 2 that the rotational contribution to the stretching term $S5$ does not vanish when the indices are contracted in Eq. (2.9). However, in the nearly homogenous core region where the vorticity ratio $S \approx -1.0$, the two parts $S5_{ij}^I$ and $S5_{ij}^{II}$ due to mean flow stretching and rotational stretching, respectively, cancel out. The enstrophy budget in Fig. 16(d) is included here to enable a qualitative comparison with the results from the channel flow simulations by Lamballais *et al.* [23]. At the anti-cyclonic side of their rapidly rotating channel they observed a balance between stretching and viscous terms.

7 Turbulence anisotropies

To further examine the anisotropy of the rotating Couette flow, anisotropy invariant maps (AIM) are presented in Fig. 17. Here, these are derived on the basis of the anisotropy tensors:

$$a_{ij} \equiv \frac{\overline{u_i u_j}}{2k} - \frac{1}{3}\delta_{ij}, \tag{7.1}$$

$$d_{ij} \equiv \frac{\varepsilon_{ij}}{2\varepsilon} - \frac{1}{3}\delta_{ij}, \tag{7.2}$$

$$v_{ij} \equiv \frac{\overline{\omega_i \omega_j}}{2\omega^2} - \frac{1}{3}\delta_{ij}. \tag{7.3}$$
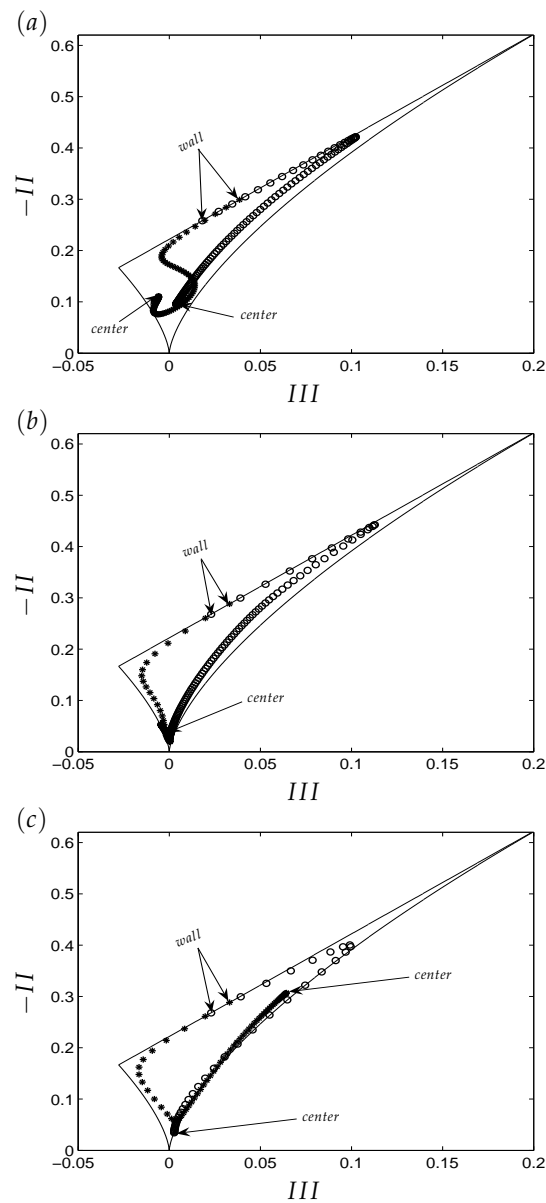
Figure 17: Anisotropy invariant maps. (a) Reynolds stress anisotropy a_{ij}; (b) dissipation rate anisotropy d_{ij}; (c) vorticity correlation anisotropy v_{ij}. Data for rotating ($*$) and non-rotating ($\circ$) Couette flow.

The so-called Lumley triangle is drawn in the (-II, III)-plane where II and III are the second and third invariant of the anisotropy tensor, see Lumley and Newman [27]. Fig. 17(a) shows that the Reynolds stress anisotropy behaves rather differently in the rotating Couette flow. Instead of tending towards the one-component limit characterized by the dominance of streamwise fluctuations as in the non-rotating case, the path from the 2D limit

in the immediate vicinity of the walls goes in the opposite direction. The anisotropy touches the boarder representing axisymmetric (rod-like) turbulence at $y^+ \approx 12$ and that of disk-like axisymmetry at $y^+ \approx 28$. Thereafter, i.e., in the quasi-homogeneous core, the anomalous anisotropy $v_{rms} > w_{rms} > u_{rms}$ prevails. The same Reynolds stress anisotropy has been observed also in rapidly rotating Poiseuille flow by Kristoffersen and Andersson [22] and Lamballais *et al.* [23, 24] as well as in homogeneous shear flows subjected to strong rotation by Salhi and Cambon [35]. The dissipation rate anisotropy d_{ij} in Fig. 17(*b*) follows a similar path as the Reynolds stress anisotropy a_{ij} in Fig. 17(*a*) and ends up with a similar anisotropy in the core region, but nearly touching the boarder signifying axisymmetric dissipation, i.e., $\varepsilon_{yy} \approx \varepsilon_{zz} > \varepsilon_{xx}$.

Also the anisotropies of the vorticity fluctuations behave similarly to the Reynolds-stress anisotropy in the near-wall region (cf. Fig. 17(*c*)), but stick to rod-like axisymmetry with $\overline{\omega_x^2}$ exceeding the two other directional vorticities throughout the core region. In the absence of rotation, however, the vorticity fluctuations in the core region are close to an isotropic state, just as in the central region of a plane Poiseuille flow. The distinctly different path followed by v_{ij} in the rotating Couette flow reflects the anomalous anisotropy of the vorticity fluctuations. The excess streamwise vorticity fluctuations depart substantially from the nearly isotropic state observed in the non-rotating Couette flow. Both Yanase *et al.* [40] and Brethouwer [9] observed very elongated and intense streamwise vortex tubes in their simulations of rapidly rotating homogeneous shear flows with $S = -1.0$. The tabulated values of v_{ij} provided by Brethouwer [9] were attained after the simulation had evolved for a time $10(dU/dy)^{-1}$ and exhibit essentially the same vorticity anisotropy as in the core region of the present rotating Couette flow. Yanase *et al.* [40] further explored the temporal evolution of high-vorticity blobs via vortex sheets into tubular vortices.

In the absence of system rotation, the paths followed by the anisotropy tensors in the three AIM-maps in Fig. 17 exhibit roughly the same shapes. In the presence of strong system rotation, on the other hand, a_{ij}, d_{ij}, and v_{ij} follow rather different paths. It is particularly noteworthy that the anisotropy of the dissipation rate tensor behaves completely different from that of the vorticity correlation tensor in the quasi-homogeneous core region.

Inspired by the arguments put forward by Nakabayashi and Kitoh [30], one may conjecture that the impact of the system rotation on the individual flow structures depends on whether the eddy size is smaller or larger than the Coriolis length scale $\delta_c = u_\tau / \Omega^F$. This motivates an inspection of the component energy spectra of the rotating Couette flow. The spectra in Fig. 18 show that the dominating role of streamwise large-scale fluctuations has been taken over by wall-normal velocity fluctuations in the center of the flow. Due to the kinematic blocking enforced by the solid surface, however, enhancement of the wall-normal fluctuations is prohibited next to the wall. Instead, spanwise fluctuations have taken over the conventional role of the streamwise fluctuations in the near-wall region. The spectra at $y/h = 1.0$ show that the conventional stress anisotropy has been inverted due to the rotation as far as the large-eddy motion is concerned whereas
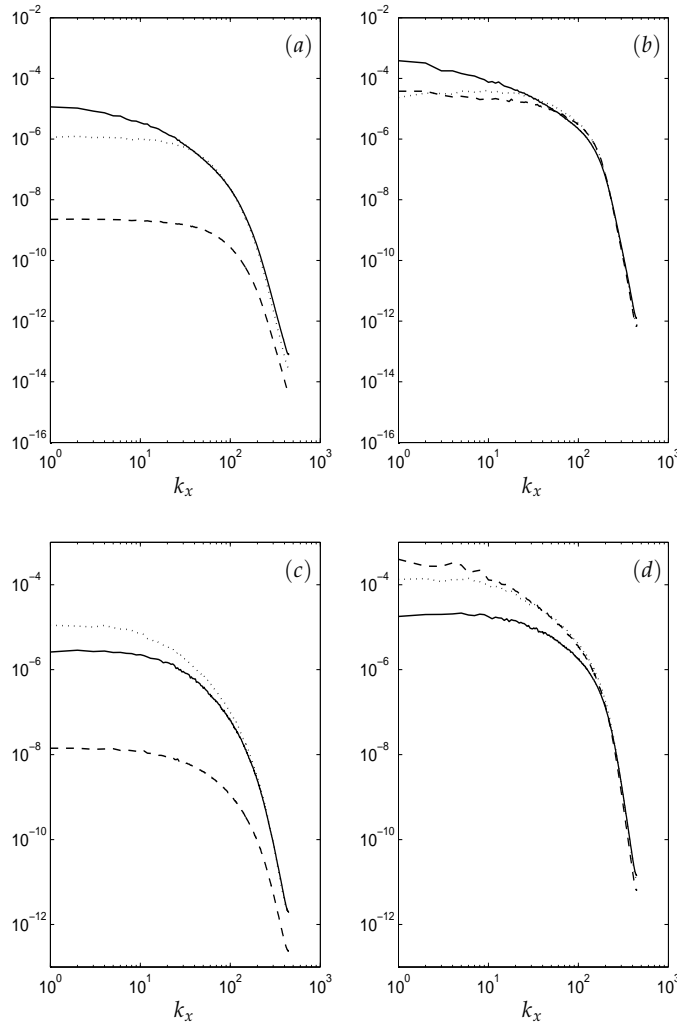
Figure 18: One-dimensional energy spectra $E_{ii}(k_x)$. (a), (c) Close to the wall at $y^+ \approx 5$; (b), (d) Near the center at $y/h = 0.98$. Results without rotation ($Ro = 0$) at the top (a,b) and with rotation ($Ro = 0.7$) at the bottom (c,d). (——) E_{uu}; (− − −) E_{vv}; (···) E_{ww}.

the isotropy of the small-scale fluctuations is retained.

The Taylor microscale ℓ_u is defined as:

$$\ell_u^2 = \frac{\overline{u^2}}{\overline{(\partial u/\partial x_j)^2}}. \tag{7.4}$$

The directional index j of the derivative is subjected to summation such that ℓ_u becomes independent of the coordinate direction. Analogous definitions are used for ℓ_v and ℓ_w. The results in Fig. 19 show that both ℓ_u and ℓ_w are fairly constant across the flow, whereas ℓ_v increases monotonically from the wall to the center of the flow. This is due to the
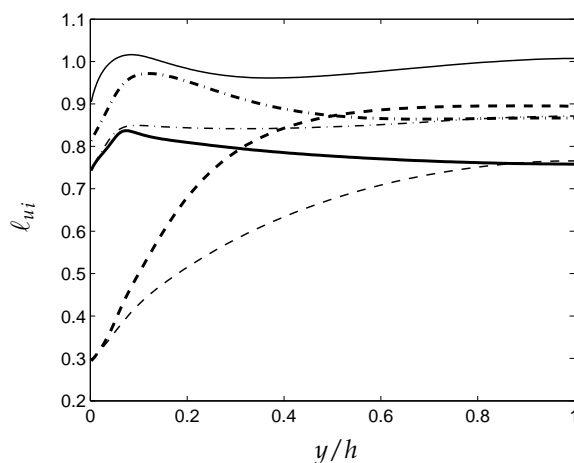
Figure 19: Taylor microscale in rotating (bold lines) and non-rotating (thin lines) plane Couette flow. (——) ℓ_u; (− − −) ℓ_v; (− · −) ℓ_w.

presence of the wall which imparts a substantial damping of wall-normal motions as compared to motions parallel with the walls. This general behaviour is therefore found irrespectively of whether the flow is rotating or not. It is interesting to observe that ℓ_v is some 15% larger in the core region in the presence of rotation than for $Ro = 0$. The Taylor microscale of the streamwise fluctuations is reduced whereas the microscale of the spanwise fluctuations is increased in the buffer region but otherwise unaffected by the rotation. The conventional scale anisotropy $\ell_u > \ell_w > \ell_v$, which reflects the conventional Reynolds stress anisotropy $u_{rms} > w_{rms} > v_{rms}$, has been inverted to $\ell_v > \ell_w > \ell_u$ in the core region for $Ro = 0.7$.

8 Concluding remarks

The plane Couette flow subjected to anti-cyclonic background rotation has been seen to develop a substantial nearly-homogeneous central core region in which the absolute mean vorticity vanishes entirely provided that the imposed system rotation is sufficiently fast. In spite of the presence of wall-layers bridging the core region with the solid walls, the core region has been found to share most of the characteristic features of the truly homogenous shear flow subjected to anti-cyclonic rotation provided that the imposed system rotation exactly outweighs the mean flow rotation.

A distinguishing feature of the present case is that the flow is statistically steady in time whereas a homogeneous shear flow is constantly evolving in time. Thus, while the mean velocity and turbulence statistics in the Couette flow become independent of time after a certain transient phase, the homogenous shear flow continuously evolves in time. In practice the computational grid often moves with the mean flow in the latter case. The inevitable skewing of the grid cells thus calls upon a re-meshing at regular

time intervals [9, 16]. Another attractive feature of the present flow is the fact that the imposed system rotation vector is consistently anti-parallel with the mean flow vorticity vector and the flow field is everywhere exposed to anti-cyclonic rotation. This contrasts with the analogous rotating Poiseuille flow, in which one part of the flow is rotating cyclonically whereas another part is subjected to anti-cyclonic rotation.

The present results have for the first time demonstrated the existence of pure turbulence in an anti-cyclonically rotating plane Couette flow, i.e., the rotation rate is sufficiently high to suppress the roll-cell instability but yet not high enough to quench the turbulence. An intuition-based conjecture suggests that $Ro = 1.0$ is an upper bound beyond which turbulence cannot be sustained. The present flow case is therefore a prominent example of so-called featureless turbulence [2]. Since the resulting mean flow becomes unidirectional in the absence of roll cells, this flow case is particularly well suited for testing of turbulence closure models aimed to be used in conjunction with the Reynolds-averaged Navier-Stokes equations.

It is widely accepted that system rotation offers a challenge to any semi-phenomenological turbulence model; see, e.g., Launder *et al.* [25], Johnston [19], Hamba [14] and Jakirlic *et al.* [17]. The present flow case should be attractive for the turbulence modeling community since the Reynolds-averaged Navier-Stokes equations and any accompanying one-point-closure model reduce to a coupled set of ODEs in the wall-normal direction. This favourable feature enables the elimination of all numerical inaccuracies and thus to pin-point any deficiencies in a model's ability to account for the effect of the Coriolis force on the turbulence field. This is only feasible in the absence of rotational-induced roll cells, i.e., in featureless turbulence as achieved for $Ro = 0.7$. Counter-rotating roll cells, which arise with moderate anti-cyclonic rotation ($Ro \leq 0.5$), inevitably contribute extra source terms to the transport equations for the second-moments of the velocity and the vorticity fluctuations, i.e., in Eqs. (2.5) and (2.9), respectively. See, for instance, Pettersson Reif and Andersson [41].

A quasi-homogeneous central core spanned about 80% of the cross-section. Here, the mean velocity profile $U(y)$ increased linearly with a slope $\approx 2\Omega^F$ such that the local vorticity ratio $S \approx -1$. Throughout this extensive region of vanishing absolute vorticity, the turbulent shear stress remained constant and the normal stress components, the vorticity tensor and the energy dissipation rate tensor exhibited abnormal anisotropies. The core region was dominated by fluctuating streamwise vorticity primarily generated by the vortex stretching mechanism $S4_{xx} = \overline{\omega_x \omega_y} dU/dy$. A 13% drag reduction resulted from the configurational changes of the turbulence field. Nevertheless, the turbulent kinetic energy level turned out to be higher than in the absence of rotation.

Acknowledgments

Appendix: Second-moment transport equations in a rotating frame-of-reference

The transport equation (2.5) for the individual components of the second-moments $\overline{u_i u_j}$ of the velocity fluctuations is written in quasi-symbolic form. The various terms on the right-hand side are defined in Cartesian tensor notation as follows:

$$P_{ij} \equiv -\overline{u_i u_k}\frac{\partial U_j}{\partial x_k} - \overline{u_j u_k}\frac{\partial U_i}{\partial x_k}, \tag{A.1}$$

$$G_{ij} \equiv -2\Omega_k^F \left(\overline{u_j u_m}\varepsilon_{ikm} + \overline{u_i u_m}\varepsilon_{jkm}\right), \tag{A.2}$$

$$D_{ij} = D_{ij}^T + D_{ij}^P + D_{ij}^V, \tag{A.3}$$

$$\Pi_{ij} \equiv \overline{\frac{p}{\rho}\left(\frac{\partial u_i}{\partial x_j} + \frac{\partial u_j}{\partial x_i}\right)}, \tag{A.4}$$

$$\varepsilon_{ij} \equiv 2\nu \left(\overline{\frac{\partial u_i}{\partial x_k}\frac{\partial u_j}{\partial x_k}}\right), \tag{A.5}$$

where the different parts of the diffusion are given by

$$D_{ij}^T \equiv -\frac{\partial}{\partial x_k}\left(\overline{u_i u_j u_k}\right), \tag{A.6}$$

$$D_{ij}^P \equiv -\frac{1}{\rho}\frac{\partial}{\partial x_k}\left(\overline{p u_i}\delta_{jk} + \overline{p u_j}\delta_{ik}\right), \tag{A.7}$$

$$D_{ij}^V \equiv \nu \left(\frac{\partial^2 \overline{u_i u_j}}{\partial x_k \partial x_k}\right). \tag{A.8}$$

Here, ε_{ijk} is the permutation or *Levi-Civita* tensor. This organization of the terms in the second-moment transport equation follows Launder *et al.* [25]. The turbulent diffusion due to velocity (D_{ij}^T) and pressure (D_{ij}^P) fluctuations and the viscous diffusion (D_{ij}^V) are labeled collectively as a single diffusion term D_{ij}.

Similarly, the transport equation (2.9) for the individual components of the second-moments $\overline{\omega_i \omega_j}$ of the vorticity fluctuations was written in quasi-symbolic form, where the various terms on the right-hand side are defined as follows:

$$T1_{ij} \equiv -\overline{\omega_i u_k}\frac{\partial \Omega_j}{\partial x_k} - \overline{\omega_j u_k}\frac{\partial \Omega_i}{\partial x_k}, \tag{A.9}$$

$$T2_{ij} \equiv -\overline{u_k \frac{\partial \omega_i \omega_j}{\partial x_k}}, \tag{A.10}$$

$$S3_{ij} \equiv \overline{\omega_i \omega_k \frac{\partial u_j}{\partial x_k}} + \overline{\omega_j \omega_k \frac{\partial u_i}{\partial x_k}}, \tag{A.11}$$

$$S4_{ij} \equiv \overline{\omega_j \omega_k} S_{ik} + \overline{\omega_i \omega_k} S_{jk}, \tag{A.12}$$

$$S5_{ij} = S5_{ij}^I + S5_{ij}^{II} \equiv (\Omega_k + 2\Omega_k^F)(\overline{s_{ik}\omega_j} + \overline{s_{jk}\omega_i}), \tag{A.13}$$

$$V6_{ij} \equiv \nu \frac{\partial^2 \overline{\omega_i \omega_j}}{\partial x_k \partial x_k}, \tag{A.14}$$

$$V7_{ij} \equiv -2\nu \left(\overline{\frac{\partial \omega_i}{\partial x_k} \frac{\partial \omega_j}{\partial x_k}} \right). \tag{A.15}$$

Here, S_{ij} and s_{ij} denote the mean and fluctuating parts of the instantaneous strain-rate tensor. Notice that $\mathbf{\Omega}^F$ denotes the constant angular velocity of the steadily rotating frame-of-reference whereas $\frac{1}{2}\mathbf{\Omega}$ is the mean angular velocity associated with the fluid motion, i.e., half the mean vorticity $\nabla \times \mathbf{U}$. The stretching term $S5_{ij}$ has been split in two parts in order to distinguish between the roles played by mean fluid rotation ($S5^I$) and system rotation ($S5^{II}$).

These expressions for the terms in the individual second-moment budgets of the fluctuating vorticity components in a rotating frame-of-reference are not available elsewhere. The above equations have been checked for consistency against the corresponding equation for the enstrophy provided by Lamballais *et al.* [23] and Liu and Lu [26]. By contraction of the indices i and j in the above terms their equation is recovered. The notion of transport (T), stretching (S), and viscous (V) terms follows Lamballais *et al.* [23], whereas the numbering refers to the order of the terms in Antonia and Kim [3], which in turn referred to equation (3.3.38) and the accompanying discussion in Tennekes and Lumley [36].

References

[1] P. H. Alfredsson and N. Tillmark. Instability, transition and turbulence in plane Couette flow with system rotation. In Laminar Turbulent Transition and Finite Amplitude Solutions, editors, T. Mullin and R. R. Kerswell, pages 173-193, Springer-Verlag, 2005.

[2] C. D. Andereck, S. S. Liu and H. L. Swinney. Flow regimes in a circular Couette system with independently rotating cylinders. J. Fluid Mech., 164 (1985), 155-183.

[3] R. A. Antonia and J. Kim. Low-Reynolds-number effects on near-wall turbulence. J. Fluid Mech., 276 (1994), 61-80.

[4] M. Barri and H. I. Andersson. Anomalous turbulence in rapidly rotating plane Couette flow. In Advances in Turbulence XI, edited by J. M. L. M. Palma and A. Silva Lopes, pages 100-102, Springer-Verlag, 2007.

[5] P. Bartello, O. Métais and M. Lesieur. Coherent structures in rotating three-dimensional turbulence. J. Fluid Mech., 273 (1994), 1-29.

[6] K. H. Bech and H. I. Andersson. Secondary flow in weakly rotating turbulent plane Couette flow. J. Fluid Mech., 317 (1996), 195-214.

[7]   K. H. Bech and H. I. Andersson. Turbulent plane Couette flow subject to strong system rotation. J. Fluid Mech., 347 (1997), 289-314.

[8]   K. H. Bech, N. Tillmark, P. H. Alfredsson and H. I. Andersson. An investigation of turbulent plane Couette flow at low Reynolds numbers. J. Fluid Mech., 286 (1995), 291-325.

[9]   G. Brethouwer. The effect of rotation on rapidly sheared homogeneous turbulence and passive scalar transport. Linear theory and direct numerical simulation. J. Fluid Mech., 542 (2005), 305-342.

[10] F. H. Busse. Bounds on the momentum transport by turbulent shear flow in rotating systems. J. Fluid Mech., 583 (2007), 303-311.

[11] C. Cambon, J.-P. Benoit, L. Shao and L. Jacquin. Stability analysis and large-eddy simulation of rotating turbulence with organized eddies. J. Fluid Mech., 278 (1994), 175-200.

[12] B. Dubrulle, O. Dauchot, F. Daviaud, P.-Y. Longaretti, D. Richard and J.-P. Zahn. Stability and turbulent transport in Taylor-Couette flow from analysis of experimental data. Phys. Fluids, 17 (2005), 095103.

[13] O. Grundestam, S. Wallin and A. V. Johansson. Direct numerical simulation of rotating turbulent channel flow. J. Fluid Mech., 598 (2008), 177-199.

[14] F. Hamba. The mechanism of zero mean absolute vorticity state in rotating channel flow. Phys. Fluids, 18 (2006), 125104.

[15] J. E. Hart. Instability and secondary motion in a rotating channel flow. J. Fluid Mech., 45 (1971), 341-351.

[16] O. Iida, Y. Tsukamoto and Y. Nagano. The tilting mechanism of a longitudinal vortical structure in a homogenous shear flow with and without spanwise shear. Flow, Turbulence Combust., 81 (2008), 17-37.

[17] S. Jakirlic, K. Hanjalic and C. Tropea. Modeling rotating and swirling turbulent flows: a perpetual challenge. AIAA J., 40 (2002), 1984-1996.

[18] J. Jeong and F. Hussain. On the identification of a vortex. J. Fluid Mech., 285 (1995), 69-94.

[19] J. P. Johnston. Effects of system rotation on turbulence structure: a review relevant to turbomachinery flows. Int. J. Rotating Machin., 4 (1998), 97-112.

[20] J. P. Johnston, R. M. Halleen and D. K. Lezius. Effects of spanwise rotation on the structure of two-dimensional fully developed turbulent channel flow. J. Fluid Mech., 56 (1972), 533-557.

[21] J. Komminaho, A. Lundblad and A. V. Johansson. Very large structures in plane turbulent Couette flow. J. Fluid Mech., 320 (1996), 259-285.

[22] R. Kristoffersen and H. I. Andersson. Direct simulations of low-Reynolds-number turbulent flow in a rotating channel. J. Fluid Mech., 256 (1993), 163-197.

[23] E. Lamballais, M. Lesieur and O. Métais. Effects of spanwise rotation on the vorticity stretching in transitional and turbulent channel flow. Int. J. Heat Fluid Flow, 17 (1996), 324-332.

[24] E. Lamballais, O. Métais and M. Lesieur. Spectral-dynamic model for large-eddy simulation of turbulent rotating channel flow. Theoret. Comput. Fluid Dynamics, 12 (1998), 149-177.

[25] B. E. Launder, D. P. Tselepidakis and B. A Younis. A second-moment closure study of rotating channel flow. J. Fluid Mech., 183 (1987), 63-75.

[26] N.-S. Liu and X.-Y. Lu. A numerical investigation of turbulent flows in a spanwise rotating channel. Comput. Fluids, 36 (2007), 282-298.

[27] J. L. Lumley and G. R. Newman. The return to isotropy of homogeneous turbulence. J. Fluid Mech., 82 (1977), 161-178.

[28] M. Manhart. A zonal grid algorithm for DNS of turbulent boundary layers. Comput. Fluids, 33 (2004), 435-461.

[29] H. K. Moffatt and A. Tsinober. Helicity in laminar and turbulent flow. Ann. Rev. Fluid Mech.,

24 (1992), 281-312.

[30] K. Nakabayashi and O. Kitoh. Low Reynolds number fully developed two-dimensional turbulent channel flow with system rotation. J. Fluid Mech., 315 (1996), 1-29.

[31] K. Nakabayashi and O. Kitoh. Turbulence characteristics of two-dimensional channel flow with system rotation. J. Fluid Mech., 528 (2005), 355-377.

[32] P. Orlandi. Helicity fluctuations and turbulent energy production in rotating and non-rotating pipes. Phys. Fluids, 9 (1997), 2045-2056.

[33] V. C. Patel and F. Sotiropoulos. Longitudinal curvature effects in turbulent boundary layers. Prog. Aerospace Sci., 33 (1997), 1-70.

[34] M. M. Rogers and P. Moin. Helicity fluctuations in incompressible turbulent flows. Phys. Fluids, 30 (1987), 2662-2671.

[35] A. Salhi and C. Cambon. An analysis of rotating shear flow using linear theory and DNS and LES results. J. Fluid Mech., 347 (1997), 171-195.

[36] H. Tennekes and J. L. Lumley. A First Course in Turbulence. MIT Press, 1972.

[37] N. Tillmark and P. H. Alfredsson. Experiments on rotating plane Couette flow. In Advances in Turbulence VI, pages 391-394, Kluwer Academic Publishers, 1996.

[38] A. A. Townsend. Axisymmetric Couette flow at large Taylor numbers. J. Fluid Mech., 144 (1984), 329-362.

[39] T. Tsukahara, H. Kawamura and K. Shingai. DNS of turbulent Couette flow with emphasis on the large-scale structure in the core region. J. Turbulence, 7 (2006), 19.

[40] S. Yanase, M. Tanaka, S. Kida and G. Kawahara. Generation and sustenance mechanisms of coherent vortical structures in rotating shear turbulence of zero-mean-absolute vorticity. Fluid Dyn. Research, 35 (2004), 237-254.

[41] B. A. Pettersson Reif and H. I. Andersson. Prediction of longitudinal roll cells in rotating plane turbulent Couette flow. Theoret. Comput. Fluid Dynamics, 14 (2000), 89-108.